

SWAP algorithm for lattice spin models

Greivin Alvaro Miranda,¹ Leticia F. Cugliandolo,^{1,2} and Marco Tarzia³

¹*Sorbonne Université, Laboratoire de Physique Théorique et Hautes Energies, CNRS UMR 7589, 4 Place Jussieu, 75252 Paris Cedex 05, France*

²*Institut Universitaire de France, 1 rue Descartes, 75005 Paris France*

³*Sorbonne Université, Laboratoire de Physique Théorique de la Matière Condensée, CNRS UMR 7600, 4 Place Jussieu, 75252 Paris Cedex 05, France*

(Dated: February 8, 2024)

We adapted the SWAP molecular dynamics algorithm for use in lattice Ising spin models. We dressed the spins with a randomly distributed length and we alternated long-range spin exchanges with conventional single spin flip Monte Carlo updates, both accepted with a stochastic rule which respects detailed balance. We show that this algorithm, when applied to the bidimensional Edwards-Anderson model, speeds up significantly the relaxation at low temperatures and manages to find ground states with high efficiency and little computational cost. The exploration of spin models should help in understanding why SWAP accelerates the evolution of particle systems and shed light on relations between dynamics and free-energy landscapes.

The slow relaxation of spin and structural glasses [1–4] poses a computational challenge because it is not feasible to investigate their progression towards equilibrium using standard numerical simulations. Efforts to overcome this slowdown have led to the development of specialized computers and numerical techniques.

Spin-glasses are interesting physical systems which also attract theoretical attention because they map to a broad range of hard combinatorial optimization problems. In the context of these frustrated magnets, methods such as parallel tempering [5], as well as the recently introduced replicated simulated annealing [6, 7], enable the equilibration of larger sample sizes compared to conventional single spin flip Monte Carlo. The special purpose Janus machine has allowed to equilibrate spin-glass models of rather large sizes, though only those with discrete variables and couplings [8]. More recently, deep reinforcement learning methods have been explored to find the ground states of finite dimensional spin-glasses [9–11].

In the context of structural glasses, Berthier *et al.* [12–14] made significant advancements over previous non-local particle exchange methods [15], achieving accelerated equilibration of several glass-forming liquids. Their breakthrough was first realized in polydisperse mixtures which still exhibit the characteristics of glass-forming liquids, and then generalized to many other models [13]. The method incorporated standard Molecular Dynamics, periodically alternated with a step in which two randomly selected particles with typically different size are exchanged using a Monte Carlo rule satisfying detailed balance. This technique, referred to as SWAP, has proven successful in equilibrating particle systems of unprecedented size, all the way down to the glass transition temperature [16].

This spectacular effect was interpreted as direct evidence against a static, cooperative explanation of the glass transition such as the one offered by the random first-order transition theory (RFOT) [17]. Yet this

claim was contested in [18] where the efficiency of SWAP was explained in terms of its ability to avoid the slowdown caused by numerous metastable local minima in the (free-)energy landscape: the non-local particle exchanges thus might be overcoming barriers quickly, in contrast to a strictly local dynamics that would necessitate cooperative rearrangements to do it. Despite the distinct (mean-field) free-energy landscapes of structural and spin glasses, they both harbor a multitude of metastable states. This suggests the potential success of a similar algorithm in accelerating the dynamics of spin glasses, models in which dynamics facilitation [19] is absent by construction.

In this Letter, we adapt the SWAP method for application to finite-dimensional spin models. In this reshaping we introduce a bypass model in which we assign a length to the spin variables, akin to the role of particle diameters in the original SWAP implementation. The exchange of constituents, in our case, the spins, will effectively mitigate the local energy barriers created by the quenched randomness, allowing us to explore configurations that would otherwise remain inaccessible.

We have chosen to focus on two two-dimensional (2D) problems for which we know the equilibrium phases and ground states. In the Supplemental Material (SM) we validate the method with a study of a clean and unfrustrated spin system with a finite-temperature second-order transition from a paramagnetic to a ferromagnetic phase. The core of this work is the study of the 2D Edwards-Anderson (EA) model, a random magnet with spin-glass properties only at zero temperature, but exceedingly long physical relaxation at low temperatures. This 2D problem is not just a theoretical construct: thin film spin-glass materials have regained experimental interest in recent years [20]. Moreover, the ground state configurations can be identified exactly with special algorithms [21, 22]. This gives us a knowledge against which we can confront the performance of our algorithm.

Concretely, we modify the Ising models by introducing associated “ Δ -models” in which the lengths of the spins are drawn initially from a pre-determined probability distribution. We then perform a single-spin-flip evolution alternating at random time-steps with a non-local exchange of spins, the swaps. The distribution of the spin-lengths remains unchanged but local energy barriers are uplifted so that the acceptance of new configurations is propitiated. In the Δ -model with uniform ferromagnetic couplings, SWAP does not improve over the standard single-spin-flip evolution of the parent Ising model (see the SM). In contrast, in the frustrated case, SWAP manages to take the Δ -model to equilibrium faster than usual implementations of parallel tempering do for the EA model at low temperatures. After instantaneous quenches, we find the ground state of the $\Delta = 2$ -Model around 2 decades faster than with parallel tempering Monte Carlo [23, 24]. This is further improved by a temperature annealing, that enables us to find at least 99% of the ground states for $\Delta \geq 0.5$.

We start from a finite-dimensional Ising Model (IM),

$$\mathcal{H} = - \sum_{\langle ij \rangle} J_{ij} \sigma_i \sigma_j, \quad \sigma_i = \pm 1, \quad i = 1, \dots, N \quad (1)$$

where $N = L^D$, $\langle ij \rangle$ indicates a sum over nearest neighbors on a D dimensional square lattice with linear size L (each pair added once) and periodic boundary conditions. In a clean ferromagnetic model the coupling strengths are all equal $J_{ij} = J > 0$. In the EA model, they are drawn from a symmetric probability distribution centered at zero, and with variance J^2 . The 2DEA model has degenerate spin-glass ground states with a gap to the lowest excitations for bimodal couplings, and only two ground states related by symmetry with a continuous spectrum of excitations in the Gaussian case. Otherwise,

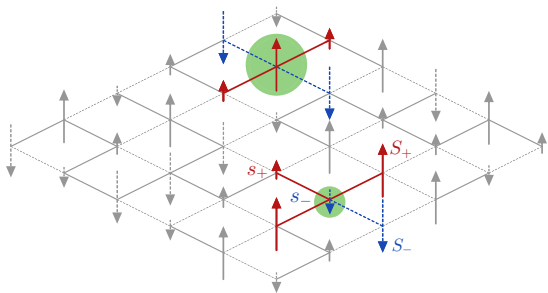


FIG. 1: Sketch of a spin configuration of the modified 2DEA model. Two spins are singled out for analysis (surrounded by green bubbles). The neighboring up and down spins are colored red and blue, respectively. The solid (red) and dashed (blue) links represent $J_{ij} > 0$ and $J_{ij} < 0$, respectively. The length of the arrows is proportional to the length of the spins, that is, the local τ_i values. They are here chosen to take only two values, for simplicity.

the model is paramagnetic at any non-vanishing temperature. The Gaussian system undergoes domain growth at $T = 0$ [25]. In the bimodal case, clusters of spins maintain their relative orientation in all ground states and form a backbone on which coarsening takes place while all other spins behave paramagnetically [26]. Single spin flip dynamics freezes at $T \lesssim 0.2$ (see Fig. SM20).

We will consider a variation of model (1) in which the spins have different amplitudes [27] or lengths,

$$\mathcal{H} = - \sum_{\langle ij \rangle} J_{ij} s_i s_j, \quad s_i = \sigma_i \tau_i. \quad (2)$$

The σ_i s are Ising variables $\sigma_i = \pm 1$ and the τ_i are independently and initially drawn from a normalized box distribution, $p_\tau(\tau_i)$, *i.e.*

$$\tau_i \in [1 - \Delta/2, 1 + \Delta/2], \quad 0 \leq \Delta \leq 2. \quad (3)$$

The average over the τ_i distribution is denoted $[\dots]$. The parameter Δ controls the spin length variation: their mean and variance are $[\tau_i] = 1$ and $[\tau_i^2] - [\tau_i]^2 = \Delta^2/12$. $\Delta \leq 2$ ensures that $\tau_i \geq 0$, and the Ising case is recovered for $\Delta = 0$. The space-varying τ_i induce random interactions between the Ising spins even in the unfrustrated case since (2) can be recast as

$$\mathcal{H} = - \sum_{\langle ij \rangle} \mathcal{J}_{ij} \sigma_i \sigma_j, \quad \mathcal{J}_{ij} = J_{ij} \tau_i \tau_j. \quad (4)$$

The new continuously varying exchanges \mathcal{J}_{ij} follow a symmetric distribution function with a gap that closes for $\Delta \rightarrow 2$, see Fig. SM16, with local spatial correlations *via* the τ_i which can be further enhanced by SWAP, see Fig. 3(c).

We proved that, in mean-field, the only effect of Δ is to modify T_c (the calculations for the fully-connected and Bethe lattice Δ -models are in the SM [28]). Additionally, the real-space RG of the Δ -model on the hierarchical lattice yields the same fixed point as the one of the EA [29–31]. These results indicate that assigning a length to the spins does not change the physics of the problem.

At each Monte Carlo (MC) sweep, with probability p the algorithm acts as follows:

$$p = \begin{cases} p_{\text{swap}} & \mapsto N \text{ (non-local) exchange attempts} \\ & s_i \leftrightarrow s_j, \\ 1 - p_{\text{swap}} & \mapsto N \text{ single spin flip attempts} \\ & \sigma_i \rightarrow -\sigma_i. \end{cases}$$

The microscopic moves are accepted with the Metropolis acceptance probability $p_{\text{acc}} = \min(1, e^{-\beta \Delta E})$, where $\beta = 1/(k_B T)$, and ΔE is the energy variation due to the i -th spin flip or the spin exchange between the i -th and j -th spins (more than one lattice spacing apart). In the following, $\langle \dots \rangle$ is an average over thermal MC noise and initial conditions of the $\{\sigma_i\}$ and $[\dots]$ stands for the average over the couplings $\{J_{ij}\}$ and the diameters τ_i .

The mechanism whereby the swaps accelerate the dynamics is exemplified in Fig. 1. For simplicity, in the sketch we use two spin lengths only, a large one (long arrows and S_{\pm}), and a smaller one (short arrows and s_{\pm}), and bimodal $J_{ij} = \pm J$ interactions. The energy barrier to flip the upper-left highlighted spin is $\Delta E = 4J(S^2 + Ss) > 0$ (as $S > 0$ and $s > 0$); therefore, this spin is blocked at low temperatures. Instead, the energy variation after an exchange of the two highlighted spins is $\Delta E = J(s^2 - S^2) < 0$ (as $s < S$). This non-local move will take place since it is energetically favorable, and it may thus help unblocking the upper-left spin and its surroundings. This mechanism will be confirmed by the analysis below.

Under single spin flips (i.e., $p_{\text{swap}} = 0$), the couplings are quenched. Instead, the s_i exchanges partially anneal the effective randomness \mathcal{J}_{ij} with speed controlled by p_{swap} . Frustrated plaquettes remain frustrated since neither the signs of J_{ij} nor \mathcal{J}_{ij} change. However, the diffusion of the τ_i can affect the magnitude of the local frustration, quantified by $f_P \equiv \prod_{(ij) \in P} \mathcal{J}_{ij}(t)$, where the product runs over the links of a plaquette P . The cumulative probability, defined as $\mathbb{P}^<(f_P < x) = \int_{-\infty}^x p_{f_P}(y) dy$ for negative f_P i.e. frustrated plaquettes, is plotted for 3 times reached with SWAP after a $T = 0$ quench in the inset of Fig. 2. SWAP reduces the magnitude of the frustration, as the probability of finding large negative values for f_P decreases with time, up until a constant functional form is reached. The two-time local correlation, $C_{\mathcal{J}}(t, t_w) = \sum_{i,j} [\langle \mathcal{J}_{ij}(t) \mathcal{J}_{ij}(t_w) \rangle] / \sum_{i,j} [\langle \mathcal{J}_{ij}^2(t_w) \rangle]$, displayed in the main part of Fig. 2, becomes stationary and $\lim_{t \gg 1} \lim_{t_w \gg 1} C_{\mathcal{J}}(t, t_w) = 1$. Effectively quenched configurations of the effective couplings $\mathcal{J}_{ij}^* = \mathcal{J}_{ij}(t_{\text{max}})$ are reached in each run after $\sim 10^5$ sweeps in a system with $L = 32$. Importantly enough, not all quenches lead to the same final \mathcal{J}_{ij}^* configuration. This is observed from the calculation of the correlation of the τ_i sampled in dif-

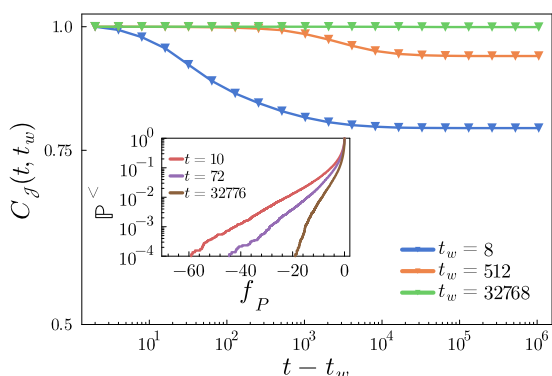


FIG. 2: The two-time correlations of the couplings \mathcal{J}_{ij} in the $\Delta = 1.5$ -model with $L = 32$ quenched to $T = 0$ evolved with SWAP ($p_{\text{swap}} = 0.1$). The waiting times t_w are given in the key. Inset: the cumulative probability of local frustrations f_P at three times after the quench.

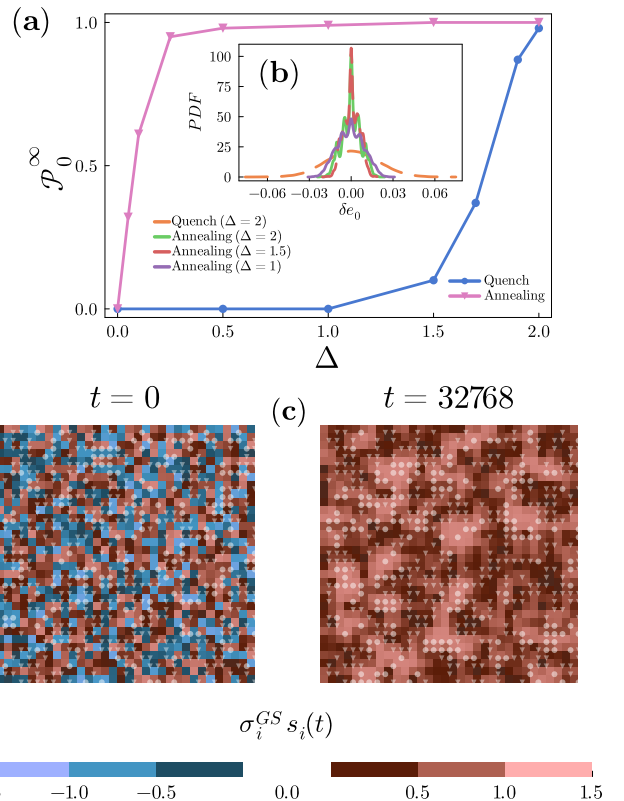


FIG. 3: (a) Asymptotic probability of reaching a ground state after a $T = 0$ quench and a quadratic annealing, starting from $T_0 = 1.0$ during $t_f \approx 10^7$ MCs. $L = 32$. Inset (b) Probability distributions of the ground state energy density differences found after $T = 0$ quenches and annealing protocols, Eq. (6), of models with different Δ . In all cases, the J_{ij} and initial lengths $\{\tau_i(t = 0)\}$ are the same, and the data are sampled over 10^3 initial Ising spin conditions $\{\sigma_i(t = 0) = \pm 1\}$. (c) The overlap of the initial (left panel) and final (right panel) s_i configuration with the ground state of the model with couplings $\mathcal{J}_{ij}^* = \mathcal{J}_{ij}(t_{\text{max}})$. The light bullets and triangles are located at frustrated plaquettes with local frustration f_P being greater or smaller than one, respectively.

ferent runs of the dynamics (according to the definition in Eq. (SM30), results not shown).

We now investigate the efficiency of the individual SWAP runs to reach the ground state of the 2DEA model with interactions \mathcal{J}_{ij}^* . With this aim we stored the couplings $\mathcal{J}_{ij}(t)$ and the Ising spins $\sigma_i(t)$. Concomitantly, we used the facility in Bonn [32] to find the unique (apart from global spin reversal) ground state σ_i^{gs} of a 2DEA model with the \mathcal{J}_{ij}^* interactions. Then, we calculated the overlap and the probability of reaching the ground state [23]

$$q(t) = \frac{1}{N} \sum_{i=1}^N \sigma_i^{\text{gs}} \sigma_i(t), \quad \mathcal{P}_0(t) = \frac{1}{N_r} \sum_{\alpha=1}^{N_r} \delta_{|q_{\alpha}(t)|, 1}, \quad (5)$$

where the index α runs over the simulation runs. Figure SM18 demonstrates that $\mathcal{P}_0^{\infty} \sim 0.5$ for $\Delta = 1$,

$\mathcal{P}_0^\infty \sim 0.75$ for $\Delta = 1.5$ and \mathcal{P}_0^∞ saturates to one for $\Delta = 2$, last blue bullet in Fig. 3. Optimization with respect to p_{swap} shows no strong dependence on p_{swap} for values in between 0.05 and 0.5, say. We use $p_{\text{swap}} = 0.1$ henceforth. However, an inconvenience resides in the fact that even in the cases in which the ground states are reached, for the same realization of the J_{ij} and initial conditions of the τ_i , different thermal evolutions produce different final configurations with a broad energy density distribution, inset in Fig. 3. Therefore, although being ground states of the 2DEA model with couplings \mathcal{J}_{ij}^* , these configurations originate from metastable states of the τ_i variables. Further optimization with respect to the τ_i is thus necessary.

In order to optimize both the τ_i and σ_i , we adopt the thermal protocol [33]

$$T(t) = T_0 (1 - t/t_f)^a, \quad (6)$$

with $T_0 = 1.0$, t_f the total number of MC-sweeps, and $a = 1$ (linear) or $a = 2$ (quadratic). SWAP is now able to find ground states 100% of the runs for almost all Δ values, pink triangles in Fig. 3. The spread of ground state energies (Gaussian distributed) narrows considerably with respect to the one of $T = 0$ quenches, inset in Fig. 3 (although it does not disappear completely). The configurations reached are ground states of models with only slightly different \mathcal{J}_{ij}^* . This is confirmed by the evolution of the self correlation of the length variables in two different runs, $\tau_i^{(1)}$ and $\tau_i^{(2)}$: after an initial decorrelation which increases with Δ , these variables progressively correlate again to reduce frustration until becoming almost identical when $T \rightarrow 0$ at the final annealing time (Fig. SM23).

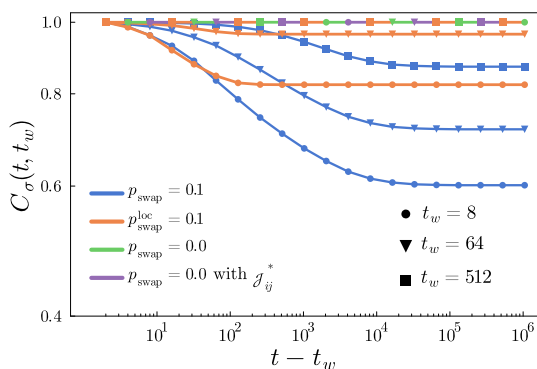


FIG. 4: The two-time Ising spin self-correlation at three waiting-times. Data for four kinds of $T = 0$ evolution of a system with $L = 32$ and $\Delta = 1.5$ starting from random initial conditions: single spin flips of the Δ model with \mathcal{J}_{ij} (i) and \mathcal{J}_{ij}^* (ii), SWAP with only local exchanges (iii) and, our main interest, SWAP with non-local ones.

Let us now compare the speed enhancement of the non-local SWAP algorithm in relation to other methods.

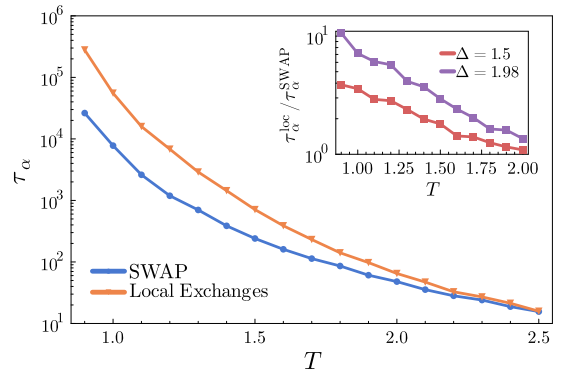


FIG. 5: Characteristic relaxation time τ_α extracted from the decay of the σ self-correlation after quenches to the target temperatures, evolved with SWAP with non-local and only local spin exchanges with the same $p_{\text{swap}} = 0.1$. In the inset, comparison of the two relaxation times, as a function of temperature for two Δ -models.

We confront it to the evolution of random initial σ_i under single spin flips of the 2DEA with (i) \mathcal{J}_{ij} couplings (in which the τ_i 's are quenched), (ii) the optimized \mathcal{J}_{ij}^* found with the quadratic annealing (in which the τ_i 's are quenched but close to the least frustrated pattern), and (iii) SWAP with only local exchanges (in which the τ_i 's are annealed). With this aim we calculated the self-correlation $C_\sigma(t, t_w) = N^{-1} \sum_{i=1}^N [\langle \sigma_i(t) \sigma_i(t_w) \rangle]$ after a $T = 0$ quench for three waiting times. The results are plotted in Fig. 4 which shows that for single spin flips freeze and the system is trapped for $L = 32$ systems. Moreover, non-local SWAP is more efficient in advancing the evolution than just local exchanges.

To precisely quantify the speed up achieved by non-local moves in comparison to only local swaps, we compared a characteristic relaxation time, τ_α , of both dynamics at rather high temperatures, to ensure equilibrium. We define this τ_α as the time for which the self-correlation has become age independent (i.e. $C(t, t_w) = C(t - t_w)$) and has decayed to 20% of its original value (i.e. $C(\tau_\alpha) = 0.2 C(t - t_w = 0)$). As can be seen in Fig. 5 the non-local spin exchanges accelerates the dynamics as we decrease the temperature, improving with respect to the local exchanges by one order of magnitude at $T = 0.9$, both dynamics are indistinguishable at higher temperatures (here, around $T \approx 2.4$).

Let us summarize our results. We adapted the SWAP algorithm to act on finite dimensional spin models. We showed that it accelerates the evolution of a 2D disordered model at very low temperatures. The method allowed us to sample ground states of an Ising spin-glass with little numerical effort. Other parameters to optimize, which we have not explored in depth yet, are $P_\tau(\tau_i)$ and the annealing scheme. The knowledge gained from the 2D models studied here will serve us to extend this study to the more interesting 3D cases with a finite tem-

perature phase transition.

In the disordered spin model, the sluggish dynamics at low temperatures is due to the intricate nature of the (free-)energy landscape. Hence, the efficiency of the SWAP algorithm in accelerating the dynamics can only be attributed to the partial smoothing of the landscape, which mitigates higher barriers as needed. This is further evidenced by the lack of acceleration in the non-disordered Ising case, characterized by a “simple” landscape. However, the acceleration achieved in the spin model is modest compared to the one accomplished in structural glasses, suggesting that facilitation [19] may also be at work in the latter case. Besides, we observe correlated patterns of spin lengths, τ_i , at low temperatures, hinting at similar phenomena in structural glasses, which calls for further investigation.

Acknowledgments. LFC acknowledges financial support from ANR-19-CE30-0014 and ANR-20-CE30-0031. We thank L. Berthier, G. Biroli, J. Kurchan, E. Marinari, F. Ricci-Tersenghi, F. Romá, J. J. Ruiz-Lorenzo and F. Zamponi for discussions and suggestions.

-
- [1] J.-P. Bouchaud, L. F. Cugliandolo, J. Kurchan, and M. Mézard, **12**, 161 (1998).
- [2] L. Berthier and G. Biroli, *Rev. Mod. Phys.* **83**, 587 (2011).
- [3] L. Berthier, G. Biroli, J.-P. Bouchaud, L. Cipelletti, and W. van Saarloos, *Dynamical Heterogeneities in Glasses, Colloids, and Granular Media* (Oxford University Press, Oxford, 2011).
- [4] G. I. Menon and P. Ray, *The physics of disordered systems* (Hindustan Book Agency, Gurgaon, 2012).
- [5] D. J. Earl and M. W. Deem, *Phys. Chem. Chem. Phys.* **7**, 3910 (2005).
- [6] C. Baldassi, C. Borgs, J. T. Chayes, A. Ingrosso, C. Lucibello, L. Saglietti, and R. Zecchina, *Proc. Nat. Acad. Sc.* **113**, E7655 (2016).
- [7] M. C. Angelini and F. Ricci-Tersenghi, *Phys. Rev. X* **13**, 021011 (2023).
- [8] F. Belletti et al., *Computing in Science & Engineering* **11**, 48 (2009).
- [9] C. Fan, M. Shen, Z. Nussinov, Z. Liu, Y. Sun, and Y.-Y. Liu, *Nat. Commun.* **14**, 725 (2023).
- [10] S. Boettcher, *Nature Communications* **14** (2023).
- [11] C. Fan, M. Shen, Z. Nussinov, Z. Liu, Y. Sun, and Y.-Y. Liu, *Nat. Commun.* **14** (2023).
- [12] L. Berthier, D. Coslovich, A. Ninarello, and M. Ozawa, *Phys. Rev. Lett.* **116**, 238002 (2016).
- [13] A. Ninarello, L. Berthier, and D. Coslovich, *Phys. Rev. X* **7**, 021039 (2017).
- [14] L. Berthier, E. Flenner, C. J. Fullerton, C. Scalliet, and M. Singh, *J. Stat. Mech.* **2019**, 064004 (2019).
- [15] L. Berthier and D. R. Reichman, *Nat. Rev. Phys.* **5**, 102 (2023).
- [16] C. Scalliet, B. Guiselin, and L. Berthier, *Phys. Rev. X* **12**, 041028 (2022).
- [17] M. Wyart and M. E. Cates, *Phys. Rev. Lett.* **119**, 195501 (2017).
- [18] L. Berthier, G. Biroli, J.-P. Bouchaud, and G. Tarjus, *J. Chem. Phys.* **150**, 094501 (2019).
- [19] D. Chandler and J. P. Garrahan, *Annual review of physical chemistry* **61**, 191 (2010).
- [20] S. Guchhait and R. Orbach, *Phys. Rev. Lett.* **112**, 126401 (2014).
- [21] A. K. Hartmann, *J. Stat. Phys.* **144**, 519 (2011).
- [22] H. Khoshbakht and M. Weigel, *Phys. Rev. B* **97**, 064410 (2018).
- [23] F. Romá, S. Risau-Gusman, A. J. Ramírez-Pastor, F. Nieto, and E. E. Vogel, *Physica A* **388**, 2821 (2009).
- [24] W. Wang, J. Machta, and H. G. Katzgraber, *Phys. Rev. E* **92**, 013303 (2015).
- [25] J. Kisker, L. Santen, M. Schreckenberg, and H. Rieger, *Phys. Rev. B* **53**, 6418 (1996).
- [26] F. Romá, S. Bustingorry, and P. M. Gleiser, *Phys. Rev. Lett.* **96**, 167205 (2006).
- [27] M. Krasnytska, B. Berche, Y. Holovatch, and R. Kenna, *J. Phys.: Complexity* **1**, 035008 (2020).
- [28] M. Mezard and G. Parisi, *Eur. Phys. J. B* **20**, 217 (2001).
- [29] B. W. Southern and A. P. Young, *J. Phys. C: Solid State Phys.* **10**, 2179 (1977).
- [30] B. Drossel, H. Bokil, and M. A. Moore, *Phys. Rev. E* **62**, 7690 (2000).
- [31] B. Drossel and M. Moore, *Eur. Phys. J. B* **21**, 589 (2001).
- [32] J. Charfreitag, M. Jünger, S. Mallach, and P. Mutzel, in *2022 Proceedings of the Symposium on Algorithm Engineering and Experiments*, edited by C. A. Phillips and B. Speckmann (2022), p. 54.
- [33] S. J. Rubin, N. Xu, and A. W. Sandvik, *Phys. Rev. E* **95**, 052133 (2017).
- [34] M. Krasnytska, B. Berche, Y. Holovatch, and R. Kenna, *Entropy* **23**, 1175 (2021).
- [35] M. Dudka, M. Krasnytska, J. J. Ruiz-Lorenzo, and Y. Holovatch, *J. Magn. Magn. Mat.* **575**, 170718 (2023).
- [36] M. Henkel and M. Pleimling, *Phys. Rev. B* **78**, 224419 (2008).
- [37] A. Bray, *Adv. Phys.* **43**, 357 (1994).
- [38] D. A. Huse and C. L. Henley, *Phys. Rev. Lett.* **54**, 2708 (1985).
- [39] A. R. Rivera, G. A. Pérez Alcázar, and J. A. Plascak, *Phys. Rev. B* **41**, 4774 (1990).
- [40] A. Sicilia, J. J. Arenzon, A. J. Bray, and L. F. Cugliandolo, *EPL* **82**, 10001 (2008).
- [41] J. L. Iguain, S. Bustingorry, A. B. Kolton, and L. F. Cugliandolo, *Phys. Rev. B* **80**, 094201 (2009).
- [42] F. Corberi, E. Lippiello, A. Mukherjee, S. Puri, and M. Zannetti, *J. Stat. Mech.* **2011**, P03016 (2011).
- [43] F. Corberi, L. F. Cugliandolo, F. Insalata, and M. Picco, *Phys. Rev. E* **95**, 022101 (2017).
- [44] R. Paul, S. Puri, and H. Rieger, *EPL* **68**, 881 (2004).
- [45] R. N. Bhatt and A. P. Young, *Phys. Rev. B* **37**, 5606 (1988).
- [46] J.-S. Wang and R. H. Swendsen, *Phys. Rev. B* **38**, 4840 (1988).
- [47] K. Hukushima and K. Nemoto, *J. Phys.: Condens. Matter* **5**, 1389 (1993).
- [48] C. K. Thomas, D. A. Huse, and A. A. Middleton, *Phys. Rev. Lett.* **107**, 047203 (2011).
- [49] F. Barahona, R. Maynard, R. Rammal, and J. P. Uhry, *J. Phys. A: Math. Gen.* **15**, 673 (1982).
- [50] F. Barahona, *J. Phys. A: Math. Gen.* **15**, 3241 (1982).
- [51] H. Takayama, K. Nemoto, and H. Matsukawa, *J. Magn.*

- Magn. Mat. **31-34**, 1303 (1983).
- [52] D. A. Huse, Phys. Rev. B **43**, 8673 (1991).
 - [53] H. Rieger, B. Steckemetz, and M. Schreckenberg, Europhys. Lett. **27**, 485 (1994).
 - [54] C. K. Thomas and A. A. Middleton, Phys. Rev. E **87**, 043303 (2013).
 - [55] N. Xu, K.-H. Wu, S. J. Rubin, Y.-J. Kao, and A. W. Sandvik, Phys. Rev. E **96**, 052102 (2017).
 - [56] L. A. Fernández, E. Marinari, V. Martín-Mayor, G. Parisi, and J. J. Ruiz-Lorenzo, J. Stat. Mech. **2018**, 103301 (2018).
 - [57] H. Khoshbakht and M. Weigel, Phys. Rev. B **97**, 064410 (2018).
 - [58] L. A. Fernández, E. Marinari, V. Martín-Mayor, I. Paga, and J. J. Ruiz-Lorenzo, Phys. Rev. B **100**, 184412 (2019).
 - [59] L. A. Fernández, E. Marinari, V. Martín-Mayor, G. Parisi, and J. J. Ruiz-Lorenzo, J. Phys. A: Math. Theor. **52**, 224002 (2019).
 - [60] H. Rieger, in *Annual Reviews of Computational Physics*, edited by D. Stauffer (World Scientific, 1995), vol. 2, p. 295.

SUPPLEMENTAL MATERIAL

Contents

A. The ferromagnetic Model	7
A.1 An equivalent Random Bond Ising Model	8
A.2 Equilibrium properties	8
A.2.1 The averaged magnetizations	8
A.2.2 The phase transition	10
A.3 Dynamical properties	11
A.3.1 Instantaneous configurations	11
A.3.2 The energy density	11
A.3.3 The space-time correlation	11
A.3.4 The growing length for the soft spins	13
A.3.5 The growing length for the Ising spins	14
A.4 Conclusions	14
B The spin-glass Model	15
B.1 An equivalent frustrated Ising model	15
B.2 The mean-field critical temperature	15
B.3 The probability of reaching the ground state after a $T = 0$ quench	17
B.4 The overlap correlation and the spin-glass growing length	17
B.5 The correlation of the τ_i variables	19
B.6 The two-time correlation	19
B.8 Measures of frustration	19
B.7 Instantaneous configurations	21

A. THE FERROMAGNETIC MODEL

In this Section we test the performance of the SWAP method when applied to a clean ferromagnetic (FM) model. Concretely, we compare the rate of approach to equilibrium of the SWAP algorithm applied to a Δ -model built upon the standard 2DIM, to the one of single spin flips applied to the unfrustrated Ising case. In both cases we work below their finite temperature critical points.

We start by generalizing the Hamiltonian of the 2DIM

$$\mathcal{H} = -J \sum_{\langle ij \rangle} s_i s_j = -J \sum_{\langle ij \rangle} \tau_i \sigma_i \tau_j \sigma_j. \quad (\text{SM1})$$

$J > 0$ and, in the rest of this Section we rescale the interactions so as to set $J = 1$. Concretely, we work with a square lattice with periodic boundary conditions. We use the summation convention in Eq. (SM1) such that the critical temperature of the Ising model is $T_c^{\text{IM}} = 2.27$.

A ferromagnetic model with spins with variable size has been considered in [27, 34, 35]. One of the motivation was to describe “structurally-disordered magnets” with two (or more) chemically different magnetic components. Specifically, the critical properties of model with variable Ising spin lengths drawn from a bimodal distribution function, was studied in detail in [35], with special

emphasis on its critical properties. We will comment on their findings when discussing the critical properties of our model.

At the initial time of the simulation we need to choose the orientation of the Ising spins σ_i and the lengths τ_i of the spins s_i . For the former we consider two cases, $\sigma_i = \pm 1$ with probability a half, mimicking an infinite temperature initial state, or $\sigma_i = 1$ for all i representing a zero temperature one. For the latter, we draw the τ_i independently from the box distribution (3).

As explained in the main text, we alternate conventional Monte Carlo (MC) updates and spin exchanges with probability p . For this model, the energy variation employed in the acceptance probability $p_{\text{acc}} = \min(1, e^{-\beta \Delta E})$, is

$$\Delta E = \begin{cases} 2s_i \sum_{j \in \partial i} s_j & \sigma_i \rightarrow -\sigma_i \\ (s_i - s_j) \left(\sum_{k \in \partial i} s_k - \sum_{k \in \partial j} s_k \right) & s_i \leftrightarrow s_j \end{cases}$$

The first line corresponds to the flipping of the i -th site and the second one to the exchange between the spins on the i -th and j -th sites, respectively, which are more than one lattice spacing apart. The symbol ∂i represents the

neighbors of the i th spin, i.e. the four nearest neighbors on the square lattice. Unless $p_{\text{swap}} = 1$, the algorithm produces non-conserved order parameter kinetics.

A.1 An equivalent Random Bond Ising Model

After the introduction of $s_i = \tau_i \sigma_i$, random interactions between the Ising spins σ_i emerge. It is straightforward to see that by separating the Ising degrees of freedom and the length-ones, the product of the latter plays the role of random couplings in the original Ising Hamiltonian (SM1). A Random Bond Ising Model (RBIM) is then recovered

$$\mathcal{H} = - \sum_{\langle ij \rangle} \mathcal{J}_{ij} \sigma_i \sigma_j \quad \text{with} \quad \mathcal{J}_{ij} = J \tau_i \tau_j, \quad (\text{SM2})$$

that is, a specific and structured distribution of the couplings \mathcal{J}_{ij} induced by the one of the τ_i lengths. This distribution is neither the box nor the bimodal one usually considered in the literature. Being the variables τ_i and τ_j i.i.d. for $i \neq j$, then $p(\mathcal{J}_{ij}) = p_\tau(\tau_i) p_\tau(\tau_j)$, so that the probability distribution function (pdf) of the new couplings can be found by means of a Mellin transform, yielding

$$p(\mathcal{J}_{ij}) = \begin{cases} \frac{1}{\Delta^2} \log\left(\frac{\mathcal{J}_{ij}}{u_-^2}\right) & u_-^2 \leq \mathcal{J}_{ij} \leq u_- u_+ \\ \frac{1}{\Delta^2} \log\left(\frac{u_+^2}{\mathcal{J}_{ij}}\right) & u_- u_+ \leq \mathcal{J}_{ij} \leq u_+^2 \\ 0 & \text{elsewhere} \end{cases}$$

with $u_- = 1 - \Delta/2$ and $u_+ = 1 + \Delta/2$.

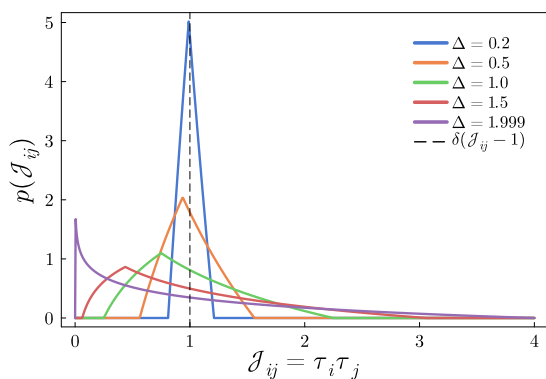


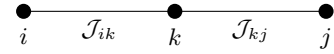
FIG. SM1: The probability distribution function of the coupling strengths $\mathcal{J}_{ij} = \tau_i \tau_j$ ($J = 1$) arising from the product of the spin-length variables. Several values of the length-controlling parameter Δ given in the key are considered.

The mean and variance are

$$[\mathcal{J}_{ij}] = 1, \quad [\mathcal{J}_{ij}^2] - [\mathcal{J}_{ij}]^2 = \frac{\Delta^2}{144} (\Delta^2 + 24). \quad (\text{SM3})$$

A plot of $p(\mathcal{J}_{ij})$ for several values of the length controlling-parameter Δ is shown in Fig. SM1, where it is clear that as we take $\Delta \rightarrow 0$ the pdf tends to a Dirac-delta distribution centered at 1 as it is expected in the hard-spin limit. These new distributions maintain $\mathcal{J}_{ij} \geq 0$ for all Δ , so frustration is avoided.

However, notice that the \mathcal{J}_{ij} are not i.i.d. variables, as for two bonds with a common spin, k , the exchanges are correlated



$$[\mathcal{J}_{ik} \mathcal{J}_{kj}] = [\tau_i \tau_k^2 \tau_j] = [\tau_i][\tau_k^2][\tau_j] = 1 + \frac{\Delta^2}{12} \\ \neq [\mathcal{J}_{ik}][\mathcal{J}_{kj}] = [\tau_i][\tau_k]^2[\tau_j] = 1. \quad (\text{SM4})$$

Therefore, the joint pdf of all couplings \mathcal{J}_{ij} is not just the product of the individual pdfs $p(\mathcal{J}_{ij})$.

We will characterize the dynamics using both interpretations: firstly, as a ferromagnetic model with soft-spins and secondly, as a RBIM with the above kind of bonds.

A.2 Equilibrium properties

In order to appropriately describe the coarsening dynamics we need to first locate the equilibrium critical temperature. In particular, we have to establish its dependence on the parameter Δ and also characterize the equilibrium properties in the spontaneous symmetry broken phase and close to the critical point. Finally, we have to prove that the equilibrium properties do not depend on the microscopic dynamic rules.

Since the equilibrium configurations below the critical point should be magnetized, for this study we initiate all simulations in σ -ordered configurations, $\sigma_i = 1$ for all i . In this way we force a positive magnetization at low temperatures. The length variables τ_i are drawn from the box distribution initially. In this way we sample different positively magnetized initial configurations of the s_i soft spins.

A.2.1 The averaged magnetizations

Two magnetization densities can be defined,

$$m_s = \frac{1}{N} \sum_{i=1}^N [\langle s_i \rangle], \quad (\text{SM5})$$

$$m_\sigma = \frac{1}{N} \sum_{i=1}^N [\langle \sigma_i \rangle], \quad (\text{SM6})$$

where the angular brackets denote average over thermal noises and the square brackets average over the distribution of the τ_i s. If one assumes that, in equilibrium, the

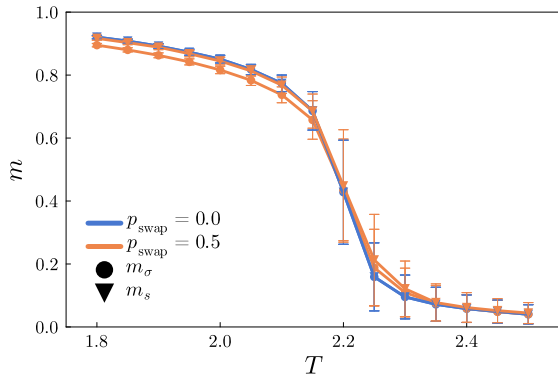


FIG. SM2: The temperature dependence of both equilibrium magnetization densities (SM5) and (SM6) in the FM model with $L = 160$ and $\Delta = 1$. A hundred zero temperature, completely ordered, initial conditions with different choices of the τ_i variables were evolved with both single-spin flip dynamics and the SWAP method with $p_{\text{swap}} = 0.5$ during $\mathcal{T} = 2^{16}$ MC-sweeps. After this time, considered to be sufficient for equilibration, we sampled the magnetization densities at 10^4 MC-sweeps. The small difference between the σ and s magnetization densities drops at high temperatures, as expected for the convergence of $m_\sigma = m_s$ to zero in the paramagnetic phase. Here and in all other plots the errorbars are estimated from the standard deviations.

average $[\langle \tau_i \sigma_i \rangle]$ factorizes as $[\tau_i][\langle \sigma_i \rangle]$, and using the fact that $[\tau_i] = 1$ (for $L \rightarrow \infty$), then

$$m_s = \frac{1}{N} \sum_i [\tau_i][\langle \sigma_i \rangle] = m_\sigma \quad \forall T, \Delta. \quad (\text{SM7})$$

This hypothesis is put to the test in Fig. SM2 where we plot both magnetization densities for an equilibrated $L = 160$ lattice and a not too strong disorder, $\Delta = 1$. The data show a very small systematic deviation, with $m_\sigma \leq m_s$, suggesting that there might be a weak correlation between the τ_i and σ_i variables along the evolution, disappearing at high temperatures when the paramagnetic disordered phase prevails with $m_s = m_\sigma = 0$. Indeed, the difference is due to the fact that thermal fluctuations tend to favor the reversal of shorter spins in the soft-spin case, since these flips cost less energy than the ones of longer spins, and hence m_s is slightly higher than m_σ in the ordered phase. (The same features are visible within the domains in the out of equilibrium snapshots in Fig. SM8.)

In Fig. SM2 we show equilibrium data obtained with the two microscopic dynamics under study, pure single spin-flip and SWAP. The static equilibrium properties are blind to the choices $p_{\text{swap}} = 0.5$ and $p_{\text{swap}} = 0$. The equivalence between the datasets built with the two dynamic rules can be verified for other values of p_{swap} in the range $0 \leq p_{\text{swap}} < 1$ and other values of Δ .

The distribution of the spin s_i values at three times, $t = 0$ and two subsequent ones, for evolutions that led to a positive magnetized domain are shown in Fig. SM3.

The $t = 0$ data are the distribution of the spin-lengths (3), multiplied by ± 1 . The evolution drives the system to positive magnetization and the weight of the pdf progressively moves to the positive support. Note that the two peaks are not symmetric around their mid-points for $t > 0$.

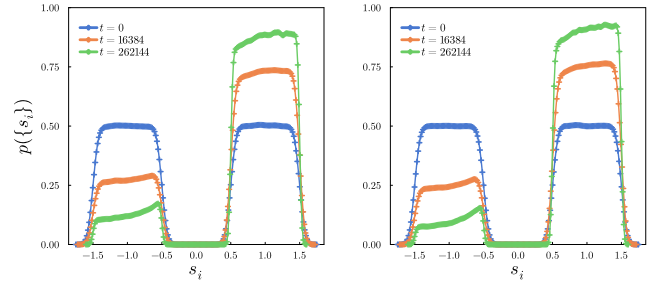


FIG. SM3: Probability distribution of the spins s_i after a quench to $T = 0.77 T_c$ from an infinite temperature initial condition, with (left) single-spin-flip kinetics and (right) SWAP dynamics ($p_{\text{swap}} = 0.5$). Data were sampled using 50 realizations of the τ_i s, with $L = 128$ and $\Delta = 1$.

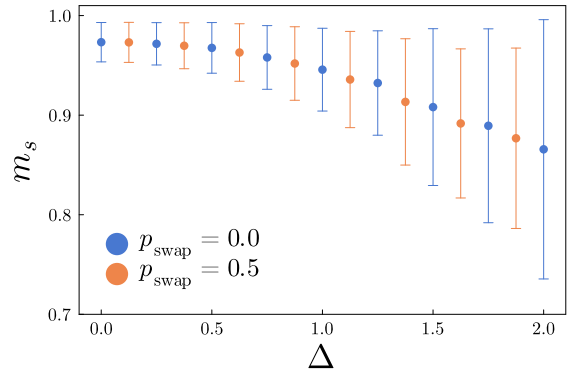


FIG. SM4: The Δ dependence of the spin s magnetization density for $L = 16$ using both kinds of dynamics. The temperature is set to $T = 1.67$ in all cases which corresponds to $0.74 < T/T_c < 0.84$ depending on the Δ considered. The equilibration time was set to 2^{18} MC-steps and data points and error bars were calculated using initial states with $\sigma_i = 1$ and 800 choices of the τ_i .

The relaxation time depends on the size of the system, temperature and the length-controlling parameter (or disorder-width), $t_{\text{eq}}(L; T, \Delta)$. Therefore, by increasing L to reduce finite size effects we are in turn increasing the relaxation time, and this makes equilibrium harder to access. In order to test the equilibrium properties at large values of Δ and, in particular, the fact that they do not depend on the microscopic dynamics, it is convenient to use small L . In Fig. SM4 we compare the Δ dependence of the equilibrium magnetization obtained with single spin flip and SWAP dynamics. Just a few averaged values show a deviation, with the SWAP ones being slightly below the single spin flip ones. This differ-

ence is not systematic and in any case very weak so we do not consider it relevant.

A.2.2 The phase transition

A second order ferromagnetic-paramagnetic transition separates magnetized and paramagnetic phases at a Δ dependent T_c . The Binder Cumulant, defined as

$$g_L^s = 1 - \frac{\left[\left\langle \left(\sum_{i=1}^N s_i \right)^4 \right\rangle \right]}{3 \left[\left\langle \left(\sum_{i=1}^N s_i \right)^2 \right\rangle \right]^2}, \quad (\text{SM8})$$

allows one to pin-down the critical point. It locates the critical temperature where the g_L^s data for different L cross, as displayed in Fig. SM5. We find $T_c(\Delta = 0) \sim 2.27$ in good agreement with T_c^{IM} . Then, $T_c(\Delta = 1) = 2.17$, a slightly lower value than T_c^{IM} . In Fig. SM6 we plot the full Δ dependence of the critical temperatures estimated from the crossing of the Binder parameter. The continuous line is a linear fit which represents the data rather accurately. The range of variation of T_c , 2.05 – 2.27, with the parameter $\Delta \in [0, 2]$ is of the same order as the one found in other works for the conventional RBIM with a box distribution of couplings and $[J_{ij}] = 1$ [36]. The analysis of the Binder cumulant of the magnetization m_σ and the two equilibrium magnetizations obtained with the SWAP method yield a $T_c(\Delta)$ which is equivalent to this one within error bars.

We have also performed a high temperature series expansion analysis (not shown) that tends to confirm that $T_c(\Delta)$ decreases with increasing Δ .

With the critical temperature and its dependency on Δ assessed, we proceed to probe the equilibrium behavior around criticality at $T_c(\Delta)$, and compare it to that of

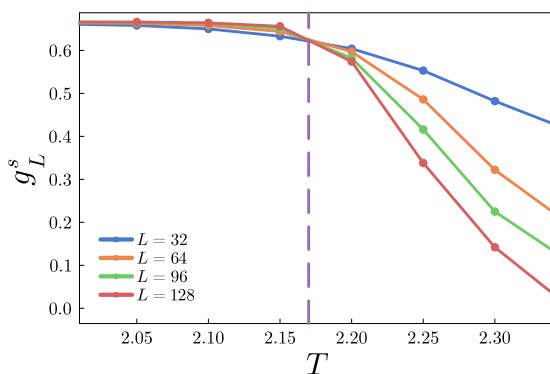


FIG. SM5: Binder cumulant's temperature dependence for the equilibrium spin s magnetization defined in Eq. (SM8) obtained with single spin flip dynamics and $\Delta = 1$. The results are equivalent for equilibrium data obtained with the SWAP evolution with $p_{\text{swap}} = 0.5$.

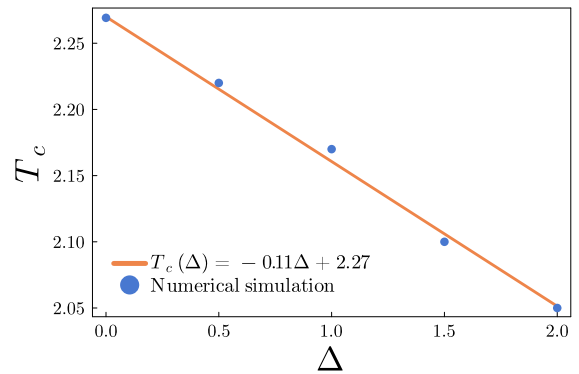


FIG. SM6: The critical temperature T_c estimated with MC simulation (datapoints) and a linear fit (curve) against Δ . The 2DIM critical value is found at $\Delta = 0$. The variation of T_c with Δ is quite weak.

the 2D pure ferromagnetic Ising universality class, for which the magnetization and correlation length critical exponents are

$$\beta = 0.125, \quad \nu = 1, \quad (\text{SM9})$$

respectively. In Fig. SM7 the equilibrium magnetizations m_s of the model with $\Delta = 1$ and different system sizes are scaled using the Ising values (SM9). The data fall on a single master curve, confirming that the critical properties of the 2DIM are preserved in the Δ -model.

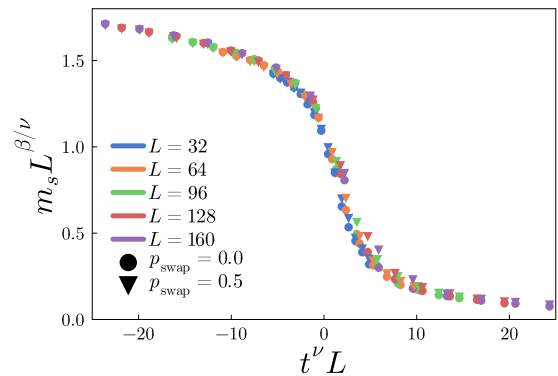


FIG. SM7: Critical scaling of the equilibrium magnetization density m_s , with $t \equiv (T - T_c)/T_c$ the reduced temperature. $\Delta = 1$. We fixed the critical exponents to the values of the clean ferromagnetic 2DIM, $\beta = 1/8$ and $\nu = 1$, and we used the estimated value of T_c for $\Delta = 1$.

In [35] the critical properties of this very same model with a bimodal distribution of lengths was studied analytically and numerically. It was shown in this paper that, apart from a special length distribution, in all other cases the criticality is the one of the 2D dilute Ising model. According to the Harris criterium, the 2D dilute Ising model is marginal and the critical exponents

(apart from logs) are the same as the ones of the 2DIM.

A.3 Dynamical properties

Having checked that the equilibrium properties of the Δ -model do not deviate significantly from the ones of the clean ferromagnetic Ising universality class, we proceed to study the domain growth. We start the dynamics from an infinite temperature initial configuration and we perform an instantaneous sub-critical quench. Studying the coarsening phenomena in this set-up will provide us with a direct survey of the microscopic evolution, hence letting us contrast the efficiency of the SWAP method to the one of the standard single-spin-flip kinetics.

A.3.1 Instantaneous configurations

We first present snapshots of the system domains along the Monte Carlo evolution. As with the magnetization densities, there are two ways to analyze the domains: 1) to consider the s_i spins as a whole, keeping track of both their sign and length, or 2) to isolate the Ising dependence σ_i . Clearly, the former carries more information than the latter.

Snapshots of the s_i spins obtained with single spin flip and $p_{\text{swap}} = 0.5$ SWAP dynamics, are displayed in Fig. SM8 top and bottom, respectively. As we lost the binary description of the spin variables, we add a color heat map to distinguish between the different local spin lengths.

As in any domain growth process the size of the domains increases with time. However, here, there are fluctuations within the domains with the same orientation but smaller absolute value than the rest (green within blue, and yellow within red). The interfaces are typically constituted by a bilayer with short spin length (green and yellow) located in between oriented regions with large spin length (blue and red). The domains built with SWAP (lower row) allow the spins with longer length to get together more easily and hence appear with darker color than the ones grown with single spin flip dynamics.

To quantify the rate at which domain growth occurs we need to measure the time-dependent typical domain size, $R(t)$, along the simulation. There are several numerical ways to get an indirect or direct measurement of this quantity. In the following we extract it from the inverse domain perimeter density and the space-time correlation.

A.3.2 The energy density

The inverse domain perimeter density,

$$R(t) = -\frac{e_{eq}}{e(t) - e_{eq}} = -\frac{e_{eq}}{\delta e(t)}, \quad (\text{SM10})$$

gives a first estimate of the growing length. The denominator $\delta e(t)$ is the distance between the time-dependent averaged energy density and the equilibrium value, $e_{eq} = \lim_{t \rightarrow \infty} e(t)$. For the clean Ising model, $R(t) \sim t^{1/z_d}$ with z_d the dynamical exponent. This in turn fixes a decay exponent for the energy density difference that would go as $\delta e \sim t^{-1/z_d}$. $z_d = 2$ for non-conserved order parameter dynamics while $z_d = 3$ for the locally conserved order parameter ones [37]. Comparing the dynamic exponents should be the simplest way to see whether one algorithm drives the system towards equilibrium faster than the other.

We calculated the equilibrium energy density in the long-time limit ($t > 2^{18}$ MC-sweeps) of runs initiated in σ -ordered initial conditions and averaged over 100 realizations of the τ_i s. The time-dependent $e(t) = [\langle \mathcal{H}(t) \rangle] / N$ was computed, instead, after quenches from completely disordered initial conditions, with parameters such that the equilibrium state is ordered. The decay of the excess energy curves is shown in Fig. SM9 in double logarithmic scale. A power law fit of the energy decays obtained with both methods leads to a time-dependent effective exponent z_{eff} reported in the caption.

After a short transient in which the effective exponent of the single spin flip dynamics is close to 2, the decay of the excess energy slows down and the effective exponent increases in time reaching a value close to 3 in the considered time window (blue data points in the main panel and the inset). The reason for this is that the variable length model has, from the point of view of the Ising spin variables σ_i , quenched random bonds. Therefore, the single spin flip dynamics feels these randomness and its evolution is slowed down, with the effective exponent developing a dependence on the disordered strength, as pointed out in the literature [36, 38–44].

The SWAP method circumvents the slowing down introduced by the variable length of the spins. The dynamical exponent of single-spin-flip kinetics of the 2DIM [37], $z_d = 2$, is recovered when one adds spin exchanges (orange data points in the main panel and the inset).

A.3.3 The space-time correlation

We now focus on the one-time spatial correlation function which also carries information on the typical domain size along the evolution. As with the magnetization densities, we either measure the space-time correlation of the complete spin-variables,

$$\begin{aligned} NC_s(r, t) &= \sum_{j=1}^N \sum_{k=1}^N [\langle s_j(t) s_k(t) \rangle] \Big|_{|\vec{r}_j - \vec{r}_k| = r} \\ &= \sum_{j=1}^N \sum_{k=1}^N [\langle \tau_j \sigma_j(t) \tau_k \sigma_k(t) \rangle] \Big|_{|\vec{r}_j - \vec{r}_k| = r} \end{aligned} \quad (\text{SM11})$$

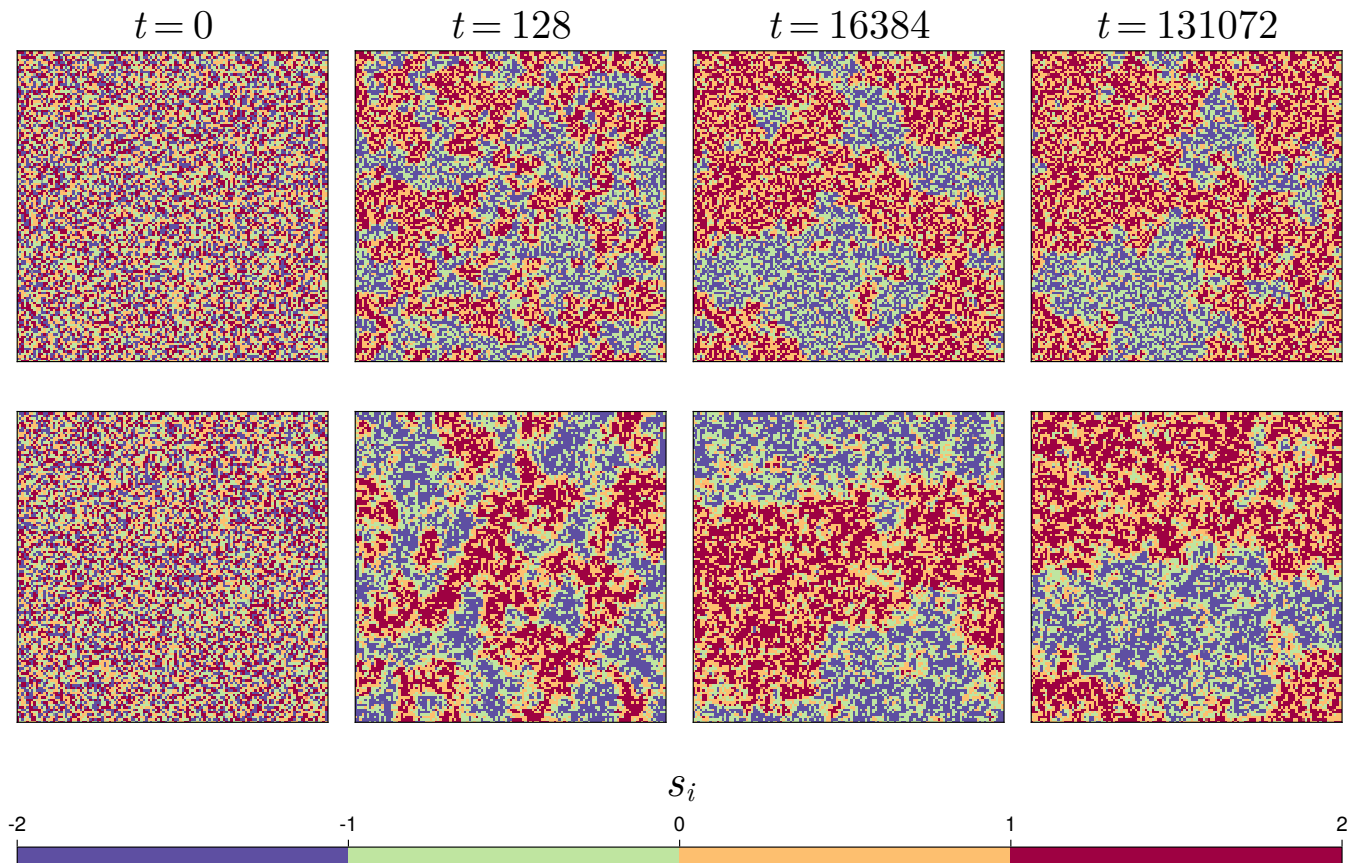


FIG. SM8: Instantaneous snapshots of the Δ -model with $\Delta = 2$ for quench at $T = 0.8T_c$. First row: single-spin-flip dynamics. Second row: SWAP dynamics. The color scale binned as indicated in the bar shows the lengths of the local spins. Note that the sizes of the domains with the same orientational order look very similar but the darkness within them different. With SWAP longer spins can get together more easily.

where the double sum over indices j and k is restricted by the condition on the distance between the spins. We normalize by the number of terms considered. Or else we measure the space-time correlations of the Ising variables, in direct correspondence with the RBIM interpretation,

$$NC_\sigma(r, t) = \sum_{j=1}^N \sum_{k=1}^N [\langle \sigma_j(t) \sigma_k(t) \rangle] \Big|_{|\vec{r}_j - \vec{r}_k| = r}. \quad (\text{SM12})$$

In both cases, $\langle \dots \rangle$ is the average over σ_i initial conditions and noise realizations of the dynamics on the one hand, and over the 2D equidistant lattice sites on the other. As stated in prior Sections, [...] represents a *disorder average* over several realizations of the lengths $\{\tau_i\}$. We note that

$$C_s(r=0, t) = \frac{1}{N} \sum_j [\tau_j^2] = 1 + \frac{\Delta^2}{12}, \quad (\text{SM13})$$

$$C_\sigma(r=0, t) = 1, \quad (\text{SM14})$$

at all times t .

Dynamic scaling states that a *single* domain length $R(t)$ should scale all correlation functions. We now study separately the correlations of the s_i and σ_i spins to confirm that this is indeed the case in this problem.

Not too close to the critical temperature, where the equilibrium magnetizations are not too low, one can estimate the typical domain size $R_{s,\sigma}(t)$ from the r such that the correlations $C_{s,\sigma}(r, t)$ decay to, say, $1/e$ of their zero distance values. A dynamic scaling regime, in which

$$C_{s,\sigma}(r, t) \sim f\left(\frac{r}{R_{s,\sigma}(t)}\right) \quad (\text{SM15})$$

is expected for $\xi_{\text{eq}} \ll r \ll L$ with ξ_{eq} the equilibrium correlation length and L the linear system size. Numerically, it is convenient to measure r along any of the two axes of the 2D lattice with PBCs.

The decay and scaling of the space-time correlation $C_s(r, t)$ in a model with $\Delta = 1$ are studied in Figs. SM10, using the SWAP method with $p_{\text{swap}} = 0.5$ and single spin-flips. At different times, the curves differ, demonstrating, once again, the out of equilibrium character of

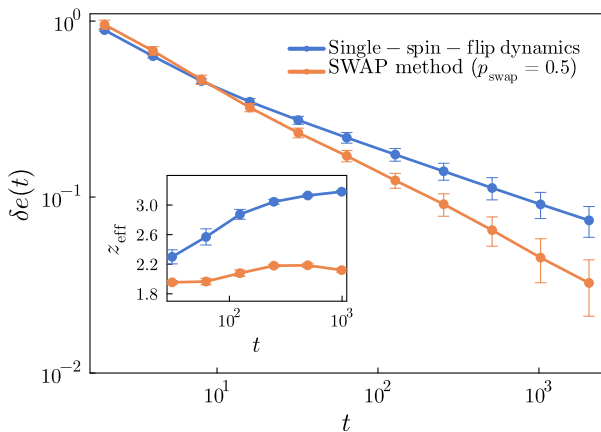


FIG. SM9: Averaged energy density relaxation of the ferromagnetic Δ -model in double logarithmic scale. Disordered initial configurations prepared at $T_0 = \infty$ were evolved at $0.55 T_c$ using single-spin flip and SWAP kinetics with $p_{\text{swap}} = 0.5$. Data correspond to $\Delta = 1$ and $L = 128$, and were averaged over 100 different initial conditions for both the $\sigma_i s$ and the $\tau_i s$. A power law fit over moving time windows including three data points yields the effective exponent z_{eff} reported in the inset.

the dynamics.

The (golden) curve, which approaches at far distances a finite constant, corresponds to the correlation decay of an ordered initial configuration that we heated up to the desired temperature $T < T_c$ and evolves in equilibrium. At very large r , the two spins in Eqs. (SM11) and (SM12) are expected to become independent and the average factorize, $\langle s_j s_k \rangle \sim \langle s_j \rangle \langle s_k \rangle$, leading to

$$\lim_{r \rightarrow \infty} C_{\text{eq}}^s(r) = [\langle s_i \rangle^2] = m_s^2, \quad (\text{SM16})$$

$$\lim_{r \rightarrow \infty} C_{\text{eq}}^\sigma(r) = [\langle \sigma_i \rangle^2] = m_\sigma^2. \quad (\text{SM17})$$

Moreover, in equilibrium the two magnetization densities are almost identical. The first of these limits is verified numerically in Fig. SM10 and the other one as well.

Dynamic scaling is checked in the inset of Fig. SM10 and it works equally fine for the σ correlations, see Fig. SM11.

The dynamical scaling master curves, $f(x)$, for C not too close to zero coincide, as can be seen in Fig. SM11. There are differences when the C s get close to zero, with oscillations for SWAP which are absent for single spin flip (somehow reminiscent of the oscillations also present when working with local-spin-exchanges as in the case of Kawasaki dynamics).

A.3.4 The growing length for the soft spins

The growing length R_s measured from the spins s space-time correlations generated with the two updating rules are studied in Fig. SM12 and Fig. SM13. In the

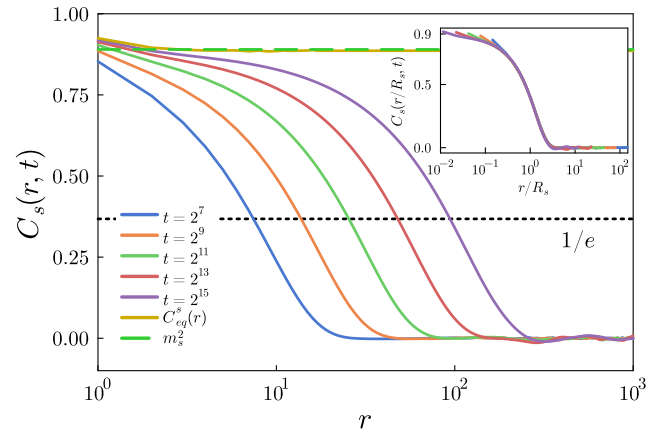


FIG. SM10: SWAP dynamics with $p_{\text{swap}} = 0.5$ of an $L = 2048$ ferromagnetic system with $\Delta = 1$, quenched from $T_0 = \infty$ to $T \approx 0.77 T_c$. Main panel: space-time correlation of the s spins at several times given in the key. The solid (gold) line is the equilibrium correlation while the dashed green line is m_s^2 in equilibrium. Inset: test of dynamic scaling with the typical domain size $R_s(t)$ estimated from $C_s(R_s(t), t) = C_s(r = 0, t)/e$, with $C_s(r = 0, t) = 1 + \Delta^2/12$. Averages are performed over 10 runs.

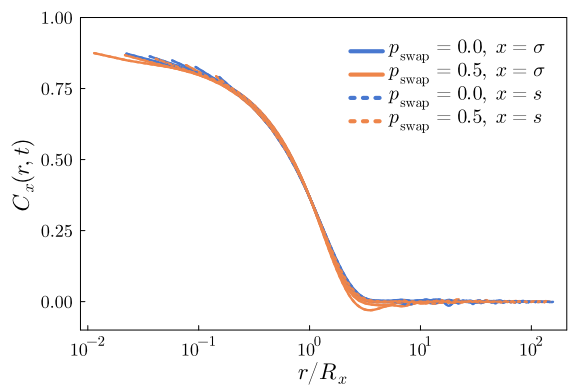


FIG. SM11: Scaling of the space-time correlations C_s and C_σ for the single-spin flip ($p_{\text{swap}} = 0$) and SWAP dynamics with $p_{\text{swap}} = 0.5$. The same master curve describes both sets of data. Same parameters as in Fig. SM10.

former, the clean ferromagnetic Ising model's $R_s = R$ is analyzed as a benchmark. In the latter, the R_s of the soft spin model is studied. As stated before, the typical domain sizes measured are fitted via a power law, with an effective exponent which depends on the width Δ ,

$$R_s(t) = \lambda t^{z_{\text{eff}}^{-1}(\Delta)}. \quad (\text{SM18})$$

λ is a non-universal parameter. The exponent z_{eff} is measured by taking averages over successive time-windows along the domain growth, as we did in the previous Section when the inverse perimeter density was calculated. The convergence of z_{eff} towards $z_d = 2$ in the clean case is verified in Fig. SM12 for single-spin-flip kinetics, while the SWAP method is unable to accelerate the dynamics,

and produces a slightly slower convergence.

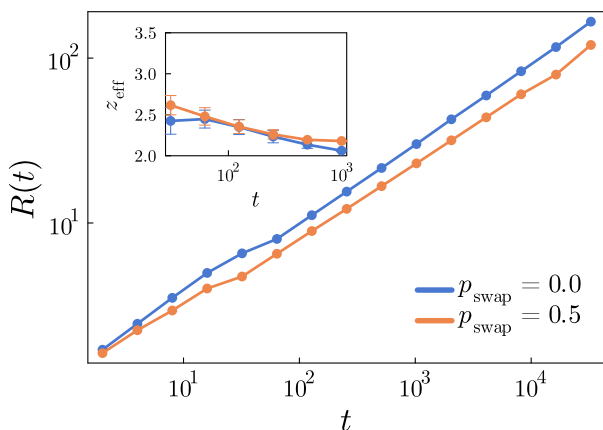


FIG. SM12: The growing length of the clean Ising model, $\Delta = 0$, with single spin flip and SWAP dynamics. The inset shows the time dependence of the effective exponent z_{eff} , measured by performing a fit of the data at (moving) six consecutive times.

In Fig. SM13 we study z_{eff} for the soft-spin model with $\Delta = 1$. When the system is evolved with single-spin-flip kinetics, we get $z_{\text{eff}} \sim 3$, and these update rules are not convenient. However, when we implement the SWAP method, the effective exponent decreases to 2.125, a value that is very close to the theoretical $z_d = 2$ of the regular 2DIM with non-conserved order parameter dynamics.

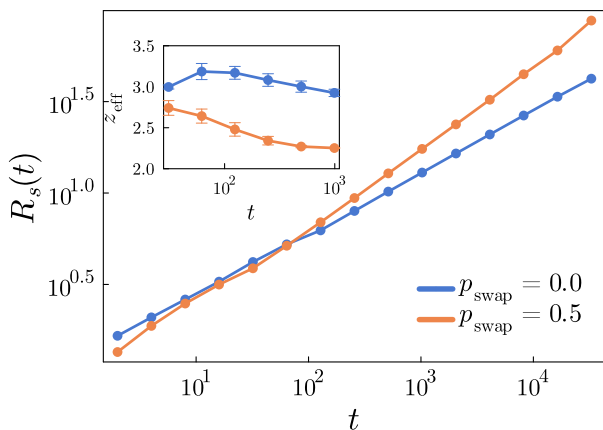


FIG. SM13: The growing length R_s (estimated from the analysis of the s spins space-time correlation) of the $\Delta = 1$ -model, with single spin flip and SWAP dynamics. Sub-critical quench to $T \approx 0.74 T_c$ and $L = 2048$. In the inset, the time dependence of the effective exponent z_{eff} , measured by performing a fit of the data at (moving) six consecutive times.

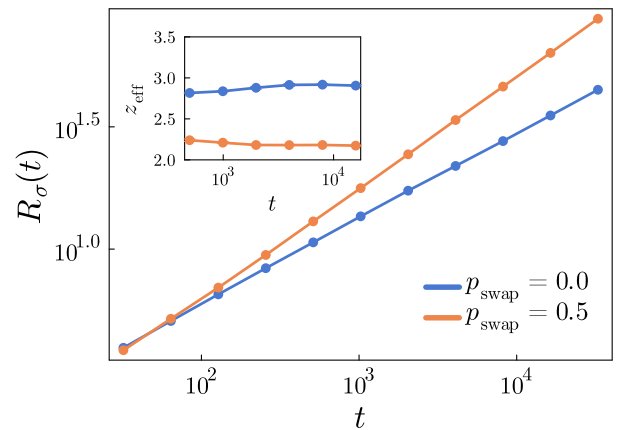


FIG. SM14: The growing length R_σ (estimated from the analysis of the Ising σ spins space-time correlation). Sub-critical quench to $T \approx 0.74 T_c$ and $L = 2048$. The inset shows the effective exponent z_{eff} variation in time, measured by performing a fit of the data at (moving) six consecutive times.

A.3.5 The growing length for the Ising spins

Now, we repeat the analysis above but this time measuring $R_\sigma(t)$. Tracking the domain growth of the Ising variables in Fig. SM14, similar conclusions are reached. The dynamic exponent remains close to 3 for the single-spin-flip updates, while z_{eff} decreases when SWAP is performed, approaching a value close to 2.25 in the numerical interval explored, which is slightly larger than $z_d = 2$ for the 2DIM with non-conserved order parameter [37].

Finally, we study the disorder dependence, Δ , of the asymptotic value of z_{eff} , which we call z_{eff}^∞ . We measure it in the last available time-interval. The results are plotted in Fig. SM15. There is a large increase of z_{eff}^∞ with the width of the spin length distribution for the single spin flip dynamics, while there is none, apart from noise, in the SWAP simulations.

A.4 Conclusions

With the SWAP dynamics one is able to obtain the equilibrium phase diagram of the Δ -model, and characterize its second order phase transition and magnetized low temperature phase. They do not vary considerably with respect to the ones of the standard 2DIM.

Concerning the out of equilibrium dynamics and further approach to equilibrium following a quench from the disordered phase, with the SWAP method one recovers the dynamic exponent of the original 2DIM, $z_{\text{eff}}^\infty \sim 2$ for any Δ . There is no improvement compared to the standard single spin flip dynamics of the original 2DIM in this unfrustrated case but, at least, there is no deterioration either. Therefore, we have validated the use of the SWAP algorithm for this model, although we do not

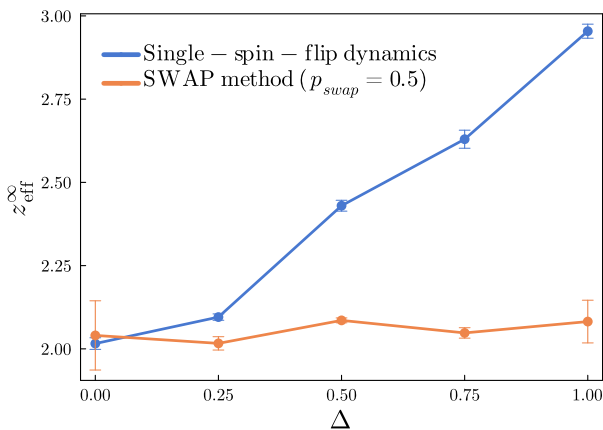


FIG. SM15: The asymptotic dynamical exponent, z_{eff}^{∞} , estimated from the effective exponent z_{eff} of the spins s growing length, in the latest time interval accessed by the simulation, against the disorder width Δ . Sub-critical quench to $T \approx 0.74 T_c$, and $L = 2048$.

improve with respect to the standard single spin flip MC using it. Instead, in cases with frustration, as we show in the main text and in the next section, the use of SWAP does accelerate the approach to equilibrium considerably.

B THE SPIN-GLASS MODEL

In this Section we provide more details and additional results on the behavior of the by-pass Δ -model that modifies the $\pm J$ 2DEA model. Concretely, in Eq. (2) we used quenched random interactions drawn from a bimodal symmetric distribution

$$p(J_{ij}) = \frac{1}{2}\delta(J_{ij} - J) + \frac{1}{2}\delta(J_{ij} + J). \quad (\text{SM19})$$

We set $J = 1$ in the numerical applications. In equilibrium this 2DEA model has no finite temperature phase transition: it has spin-glass ground states and is paramagnetic at non-vanishing temperatures [45–48]. Still, it presents a non-trivial slow relaxation towards the equilibrium paramagnetic state at low enough temperatures [21, 22, 26, 33, 49–59].

The Hamiltonian of the frustrated Δ -model takes the form

$$\mathcal{H} = - \sum_{\langle ij \rangle} J_{ij} s_i s_j = - \sum_{\langle ij \rangle} J_{ij} \tau_i \tau_j \sigma_i \sigma_j. \quad (\text{SM20})$$

For pure Ising spins, $\tau_i = 1 \forall i$, it boils down to the 2DEA model with the bimodal couplings in Eq. (SM19).

B.1 An equivalent frustrated Ising model

By following the same recipe used to analyze the ferromagnetic model, one can re-express the Hamiltonian with

randomly chosen lengths τ_i as an EA Ising spin-glass

$$\mathcal{H} = - \sum_{\langle ij \rangle} \mathcal{J}_{ij} \sigma_i \sigma_j, \quad (\text{SM21})$$

with an uncommon kind of couplings, defined as $\mathcal{J}_{ij} = J_{ij} \tau_i \tau_j$. The \mathcal{J}_{ij} are correlated through the site dependence of the $\{\tau_i\}$, similarly to what happened with the ones of the ferromagnetic model, see Eq. (SM4).

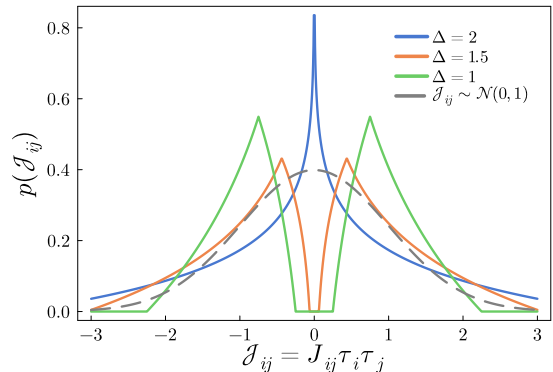


FIG. SM16: The probability distribution function of the coupling strengths $\mathcal{J}_{ij} = J_{ij} \tau_i \tau_j$, arising from the product of the spin-lengths $\tau_i \tau_j$ and the quenched couplings J_{ij} taking ± 1 values with probability a half. The dashed line represents a Gaussian distribution in normal form for comparison.

The mean and variance of the new effective couplings \mathcal{J}_{ij} are

$$[\mathcal{J}_{ij}] = 0, \quad [\mathcal{J}_{ij}^2] - [\mathcal{J}_{ij}]^2 = J^2 \left(1 + \frac{\Delta^2}{12} \right). \quad (\text{SM22})$$

Moreover, there is a persistent quenched randomness, the J_{ij} , that is unaffected by the choice of the dynamics, unlike the $\{\tau_i\}$ that remain locally unmodified only when the dynamics do not involve spin exchanges.

In Fig. SM16 we show the distribution of the couplings \mathcal{J}_{ij} induced by the one of the τ_i for three values of Δ . The usual Gaussian distribution with zero mean and unit variance is also shown for reference. The distribution of the couplings \mathcal{J}_{ij} is just two delta peaks at $\pm J$ for $\Delta \rightarrow 0$ and it progressively shrinks the gap for increasing Δ until closing it completely when $\Delta = 2$.

As explained in the main text, the frustration in the model is only determined by the J_{ij} couplings. The introduction of the spin lengths and the insofar induced \mathcal{J}_{ij} do not remove it.

B.2 The mean-field critical temperature

In mean-field (within the fully connected approximation) the critical temperature of an Ising model with *fixed* couplings \mathcal{J}_{ij} (i.e. when both the J_{ij} 's and the τ_i 's are

quenched) in equilibrium at an inverse temperature β can be estimated from the use of the TAP approach. After having conveniently scaled the \mathcal{J}_{ij} with N to ensure a good thermodynamic limit, one derives the following equations for the local magnetizations:

$$m_i = \tanh \left[\beta \sum_{\partial i} \mathcal{J}_{ij} m_j + \beta h_i - \beta^2 \sum_{\partial i} \mathcal{J}_{ij}^2 (1 - m_j^2) m_i \right]$$

The sums $\sum_{\partial i}$ indicate the spins j connected to i . Assuming a continuous phase transition and taking $h_i \sim 0$ as well, the local magnetization should be $m_i \sim 0$. If, moreover, one replaces \mathcal{J}_{ij}^2 by $[\mathcal{J}_{ij}^2]$ in the Onsager reaction term,

$$\begin{aligned} m_i &\sim \beta \sum_{\partial i} \mathcal{J}_{ij} m_j + \beta h_i - \beta^2 \sum_{\partial i} [\mathcal{J}_{ij}^2] m_i \\ &\sim \beta \sum_{\partial i} \mathcal{J}_{ij} m_j + \beta h_i - \beta^2 J^2 \left(1 + \frac{\Delta^2}{12} \right)^2 m_i. \end{aligned}$$

This equation can now be taken to the basis of eigenvectors of the matrix with elements \mathcal{J}_{ij} . Calling \vec{v}_μ the eigenvector associated to the eigenvalue λ_μ , and $m_\mu = \vec{m} \cdot \vec{v}_\mu$,

$$m_\mu \sim \beta \lambda_\mu m_\mu + \beta h_\mu - \beta^2 J^2 \left(1 + \frac{\Delta^2}{12} \right)^2 m_\mu.$$

The linear susceptibilities are

$$\chi_\mu = \left. \frac{\partial m_\mu}{\partial h_\mu} \right|_{\vec{h}=0} \sim \frac{\beta}{1 - \beta \lambda_\mu + \beta^2 J^2 \left(1 + \frac{\Delta^2}{12} \right)^2}.$$

The first susceptibility to diverge is the one associated to the largest eigenvalue λ_{\max} and this arises at

$$\beta_c = \frac{\left[\lambda_{\max}^2 - 4J^2 \left(1 + \frac{\Delta^2}{12} \right)^2 \right]^{1/2}}{2J^2 \left(1 + \frac{\Delta^2}{12} \right)^2}. \quad (\text{SM23})$$

In the Sherrington-Kirkpatrick model, the mean-field limit of the EA model, $\Delta \rightarrow 0$ and $\lambda_{\max} = 2J$. Then, $\beta_c = J^{-1}$. If, in the Δ -model, $\lambda_{\max} = 2[\mathcal{J}_{ij}^2]^{1/2}$, which seems reasonable, then

$$\beta_c \propto [\mathcal{J}_{ij}^2]^{-1/2} \Rightarrow T_c = J \left(1 + \frac{\Delta^2}{12} \right). \quad (\text{SM24})$$

In Fig. SM17 we plot, with orange data points, the critical temperature $T_c(\Delta)$ obtained from diagonalizing symmetric matrices with such elements and linear size $L = 32$ ($J = 1$). The datapoints are consistent with the quadratic dependence on Δ linking $T_c = J$ at $\Delta = 0$ and $T_c = 4/3 J$ at $\Delta = 2$.

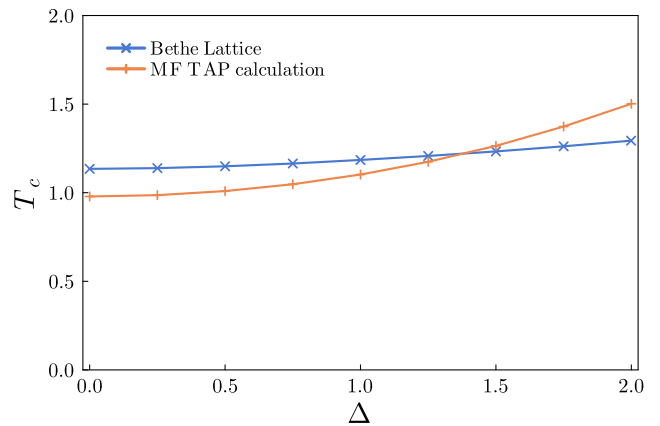


FIG. SM17: The Δ dependence of the critical temperature in mean-field. Orange data: results for the fully connected model with the TAP approach. Blue data: results for the Bethe lattice model with connectivity $k = 2$. The trend is the same and the range of variation of the critical temperature with Δ is very weak in both cases.

An alternative way to estimate the Δ dependence of the critical temperature with a mean-field approach is to place the model on a Bethe lattice with connectivity k . By defining the cavity field acting on site i produced by the effect of k neighboring spins (in the absence of its j -th neighbor), we obtain the recursive equations

$$\begin{aligned} h_{i \rightarrow j}(\tau_i) &= \\ &= \sum_{m \in \partial i / j} \frac{1}{\beta} \text{atanh} \left[\tanh(\beta J_{im} \tau_i \tau_m) \tanh(\beta h_{m \rightarrow i}(\tau_m)) \right]. \end{aligned} \quad (\text{SM25})$$

The sum excludes $m = j$. These equations admit $h_{i \rightarrow j} = 0$ as a solution on all sites, corresponding to the paramagnetic phase.

Since we will be interested in the temperature regime in the vicinity of the critical point, $T \lesssim T_c$, in which the cavity fields are small, we can expand the right-hand-side of Eq. (SM25):

$$h_{i \rightarrow j}(\tau_i) \simeq \sum_{m \in \partial i / j} \tanh(\beta J_{im} \tau_i \tau_m) h_{m \rightarrow i}(\tau_m). \quad (\text{SM26})$$

Due to the randomness of the spin-amplitudes, these equations must be interpreted as a self-consistent integral equation for the probability distribution of the local cavity fields

$$\begin{aligned} P(h|\tau) &= \\ &= \int \prod_{m=1}^k \left[\sum_{J_m} d\tau_m dh_m p_\tau(\tau_m) P(h_m|\tau_m) \right] \delta(h - \tilde{h}), \end{aligned}$$

with $\tilde{h} = \sum_m \tanh(\beta J_m \tau \tau_m) h_m$. Using the integral representation of the δ -function, one obtains the following

equation for the Fourier transform of the probability distribution

$$\hat{P}(q|\tau) = \left[\int \sum_J d\tau' p_\tau(\tau') \hat{P}(q \tanh(\beta J \tau \tau') | \tau') \right]^k,$$

Assuming that the fields follow a Gaussian distribution with variance, $\sigma_h^2 = \overline{h(\tau)^2} - \overline{h(\tau)}^2$, we have

$$\hat{P}(q|\tau) = 1 - iq\overline{h(\tau)} - \frac{q^2}{2}\overline{h^2(\tau)} + \dots$$

plugging this expression into the equation above, using the fact that $\overline{h(\tau)^n} \ll 1$ for $T \lesssim T_c$, and expanding up to second order one finds

$$\begin{aligned} \overline{h(\tau)} &= k \int \sum_J d\tau' p_\tau(\tau') \tanh(\beta J \tau \tau') \overline{h(\tau')}, \\ \overline{h^2(\tau)} &= k \int \sum_J d\tau' p_\tau(\tau') \tanh^2(\beta J \tau \tau') \overline{h^2(\tau')} \\ &\quad - \frac{k-1}{k} \overline{h(\tau)}^2. \end{aligned}$$

For $\overline{h(\tau)} = 0$ we are interested in the second equation, that defines a linear integral operator $f(\tau) = \int d\tau' \Gamma(\tau', \tau) f(\tau')$, with $f(\tau) = \overline{h^2(\tau)}$ and the (non-symmetric) kernel

$$\Gamma(\tau', \tau) = k \sum_{J=\pm J} p_\tau(\tau') \tanh^2(\beta J \tau \tau'). \quad (\text{SM28})$$

Therefore a solution of Eq. (SM27) with a non-vanishing function $\overline{h^2(\tau)}$ only exists if such integral operator has an eigenvector with eigenvalue 1. For the specific case of the box distribution of width Δ we have diagonalized the integral operator numerically for $J = 1$ and $k = 2$, for several values of β and Δ , on a grid of 2048×2048 intervals. The results for the critical temperature are reported in blue Fig. SM17. Note that for $\Delta \rightarrow 0$ the critical temperature tends to the Bethe lattice value for the Ising spin-glass, $\beta_c J = \text{atanh}(\sqrt{1/k}) \sim 0.88$, that is $T_c = 1.13 J$. The increasing trend is the same as the one derived in the fully connected model with the TAP method. The range of variation of the critical temperature with Δ is very weak in both cases.

B.3 The probability of reaching the ground state after a $T = 0$ quench

We investigate the efficiency of SWAP to reach the ground states of the 2DEA model with the interactions \mathcal{J}_{ij}^* obtained at the latest time reached after a zero temperature quench with SWAP.

The main panel in Fig. SM18 displays $\mathcal{P}_0(t)$ for three values of Δ and $p_{\text{swap}} = 0.5$. In all cases, after a fast increase ending at $t \lesssim 10^3$ MCs, $\mathcal{P}_0(t)$ saturates to a \mathcal{P}_0^∞

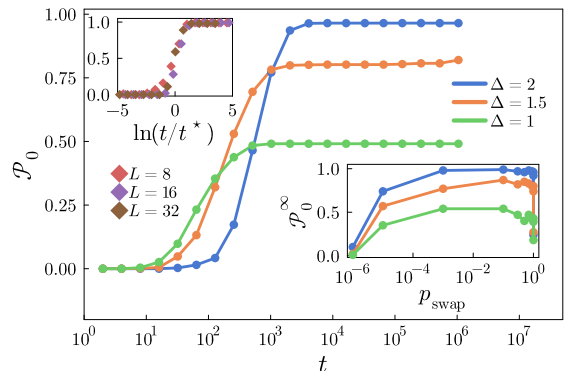


FIG. SM18: The probability of reaching the ground state of the Δ -model with $\mathcal{J}_{ij}^* = \mathcal{J}_{ij}(t_{\text{max}})$, in systems with $L = 8$ after zero temperature quenches. Main panel: three Δ values given in the right key and $p_{\text{swap}} = 0.5$. For $\Delta = 2$, 96.5% of the runs find a ground state. Lower inset: the asymptotic value against the parameter p_{swap} for $\Delta = 2$. Upper inset: Scaling with $t^*(L) = 1.25 L^{3.75}$ of the data for $\Delta = 2$, $p_{\text{swap}} = 0.1$ and three system sizes specified in the left key.

which increases with Δ and gets very close to 1 for $\Delta = 2$. Further optimization of the algorithm achieved by gauging p_{swap} is studied in the lower inset which shows the dependence of \mathcal{P}_0^∞ on p_{swap} in the $\Delta = 2$ -model. For intermediate values, $0.1 \lesssim p_{\text{swap}} \lesssim 0.9$, \mathcal{P}_0^∞ remains approximately constant apart from numerical noise, and it decays to zero at the two extremes of either non-local spin exchanges ($p_{\text{swap}} \rightarrow 1$) or pure single-spin-flips ($p_{\text{swap}} \rightarrow 0$). Finally, we checked the dependence on system size using $\Delta = 2$ and $p_{\text{swap}} = 0.1$. The curves are similar and the percentage of ground states found is independent of L . The upper inset shows the scaling of \mathcal{P}_0 against $t/t^*(L)$ with $t^*(L) \sim 1.25 L^{3.75}$.

B.4 The overlap correlation and the spin-glass growing length

The overlap or four spin correlation is defined as

$$NC_4(r, t) = \sum_{\substack{i,j=1 \\ |\vec{r}_i - \vec{r}_j|=r}}^N \left[\left\langle \sigma_j^{(1)}(t) \sigma_j^{(2)}(t) \sigma_i^{(1)}(t) \sigma_i^{(2)}(t) \right\rangle \right] \quad (\text{SM29})$$

and the characteristic length over which it decays defines the spin-glass ordering length. It is here estimated from $R_\sigma(t) = 2 \int_0^\infty dr C_4(r, t)$, as defined in [53].

The Metropolis dynamics of the 2DEA at $T \simeq 0.5$ yield a super exponential decay, $C_4 \sim e^{-(r/R_\sigma(t))^\beta}$, with $\beta > 1$. The spin-glass length scales as $R_\sigma(t) \sim (t/\tau(T))^{1/z}$ with $z \sim 7$ and an Arrhenius characteristic time $\tau(T)$ at these relatively high temperatures [56].

The spatial dependence of C_4 , at different times, is studied in Fig. SM19 at $T = 0.5$ and $T = 0.1$. At high

temperatures SWAP on the $\Delta = 1$ model yields equivalent results to the single-spin flip evolution of the original $\Delta = 0$ model. At the longest time $t \sim 10^6$ considered the growing length is of the order of 20, say, while the system's linear size is $L = 512$.

At low temperatures instead SWAP is much more efficient in building long-range correlations, even between copies that may have evolved towards different effective random couplings \mathcal{J}_{ij} , than the single-spin flip evolution of the original $\Delta = 0$ model. Still, the correlations obtained with SWAP at the same time $t \sim 10^6$ decay faster than at higher T , reaching a shorter $R_\sigma(t)$.

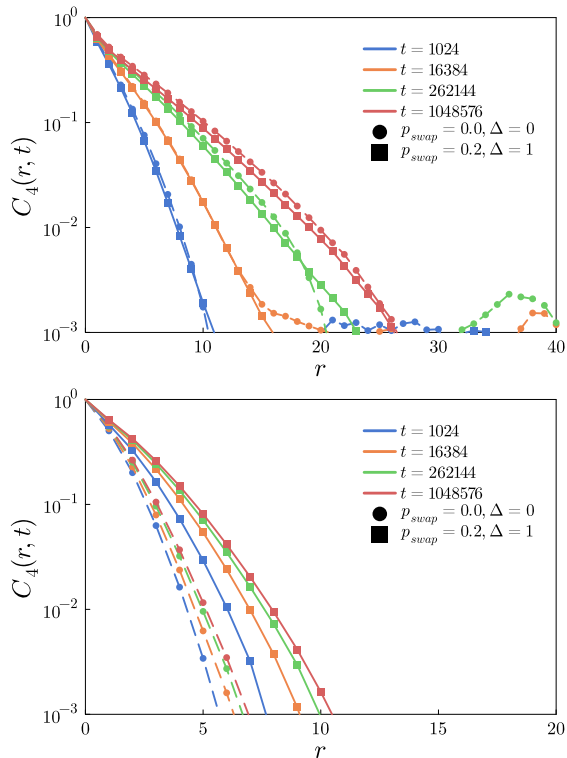


FIG. SM19: Overlap correlation $C_4(r, t)$, Eq. (SM29), versus the Cartesian distance r for several times given in the keys. $L = 512 \pm J$ 2DEA ($\Delta = 0$) model evolved with single-spin and $\Delta = 1$ model evolved with SWAP and $p_{\text{swap}} = 0.2$. Data for $T = 0.5$ (above) and $T = 0.1$ (below). While single spin flips and SWAP yield equivalent results at high temperature, the latter builds longer correlations at low temperature.

For single-spin-flip dynamics, the growing length of the $\pm J$ 2DEA Ising model, which we simply call $R(t)$ in Fig. SM20, freezes at low enough temperatures ($T \leq 0.2$), saturating at a very short value [60]. The dynamic exponent, plotted in the inset of the same figure, diverges. By increasing the temperature the plateau is surpassed and the evolution persists. The latter growth can be described with the power-law $t^{1/z_{\text{eff}}}$, as in Eq. (SM18), and z_{eff} converges to a value close to 8.5 at T larger than 0.3, say.

Finally, in Fig. SM21 we compare the performance of

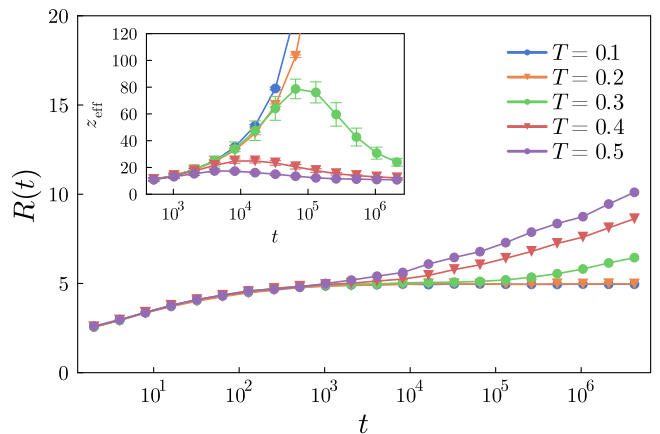


FIG. SM20: Typical growing length in the $\pm J$ 2DEA model with $L = 512$ evolved with single spin flip dynamics at several temperatures displayed in the key. The inset shows the time dependence of the dynamical exponent z_{eff} : it converges to ~ 8.5 after the saturation of the growing length at the value $R_p = 4.483 \pm 0.004$ is superseded at high-enough temperatures ($T > 0.2$).

SWAP with different values of the parameter p_{swap} to the one of the single spin flip updates when applied to the $\Delta = 1$ model at high temperature. The data in the figure demonstrate that the two methods perform similarly.

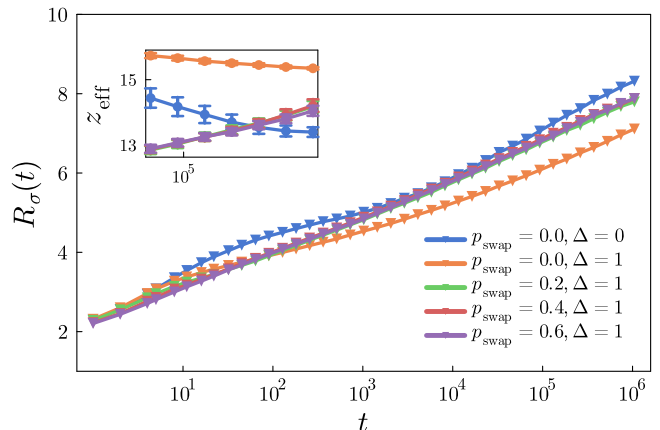


FIG. SM21: Typical growing length of the frustrated soft spin model with $L = 512$ and $\Delta = 1$, evolving with SWAP and single spin flip dynamics at a relatively high temperature, $T = 0.5$. The growth in the $\pm J$ 2DEA with single spin flip dynamics is plotted for comparison. Several values of p_{swap} were used. The inset shows the time evolution of the dynamical exponent. In all cases a similar long-time limit, close to 8, is reached.

We henceforth focus on $T < 0.3$. In Fig. SM22(a) we display the spin-glass length for the $\Delta = 0$ and $\Delta = 1$ models quenched to $T = 0.1$, and evolved with single spin flip and SWAP dynamics. At such low temperature the single spin flip dynamics of the $\Delta = 0$ model freeze and the spin-glass length saturates to $R_\sigma \sim 5$ (blue

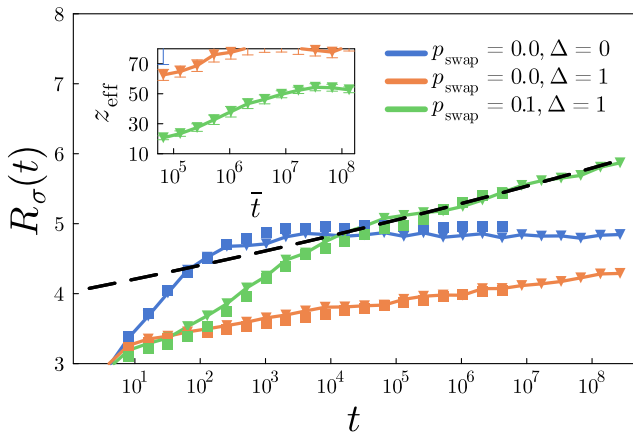


FIG. SM22: Spin-glass growing length in systems with $L = 32$ (triangles) and $L = 512$ (squares) quenched to $T = 0.1$. The three curves compare the single spin flip evolution of the Ising ($\Delta = 0$) and soft ($\Delta = 1$) models to the SWAP one of the latter. The inset displays the dynamical exponent z_{eff} as a function of \bar{t} , the center of the time interval over which the algebraic fit was performed (with 12 data points, and $L = 32$). In dashed black is the fit with $z_{\text{eff}} = 49.5(86)$ and amplitude $A = 3.94(2)$.

data). Instead, both single spin flips (orange) and SWAP (green) of the $\Delta = 1$ model accelerate the dynamics at long times, with the latter becoming more efficient in the last four time decades. We estimated running effective exponents from fits over a moving window with 12 data points (inset). Within numerical accuracy z_{eff} converges to $z_{\text{eff}}^{\infty} \sim 49$. The dashed line is the algebraic law $A t^{1/z_{\text{eff}}^{\infty}}$.

However, the long-time configurations are not in equilibrium. First, the maximal length $R_{\sigma} \sim 6$ for $L = 32$ is far from $L/2$. Second, the τ_i variables, which are also dynamical under SWAP, are still evolving. Hence, $\sigma_i^{(1)}$ and $\sigma_i^{(2)}$ may be optimized with respect to different \mathcal{J}_{ij} and thus not really inform us about the performance of the algorithm and measurement in taking one system close to equilibrium.

B.5 The correlation of the τ_i variables

In Fig. SM23 we plot the time evolution of the correlation

$$C_{\tau^{(1)}\tau^{(2)}}(t) = \frac{\left[\frac{1}{N} \sum_{i=1}^N \tau_i^{(1)}(t) \tau_i^{(2)}(t) \right] - 1}{\left(1 + \frac{\Delta^2}{12} \right) - 1} \quad (\text{SM30})$$

where $\tau_i^{(1)}$ and $\tau_i^{(2)}$ are the values of the length variables in two runs of the same quenched disordered model (same J_{ij}) starting from the same initial condition of the Ising spins and length variables and evolved with different

Monte Carlo noises. At equal times $C_{\tau^{(1)}\tau^{(2)}}(t=0) = 1$ by definition since $\tau_i^{(1)}(0) = \tau_i^{(2)}(0)$ and $[\tau_i^2] = 1 + \Delta^2/12$. If for $t \rightarrow \infty$ the $\tau_i^{(1)}$ and $\tau_i^{(2)}$ lengths fully correlate again, then 1 should be recovered in this limit as well. This is confirmed in Fig. SM23 where this time-dependent correlation is shown for various values of Δ in a system with $L = 16$ annealed following the protocol (6) from $T_0 = 0.5$ to zero temperature.

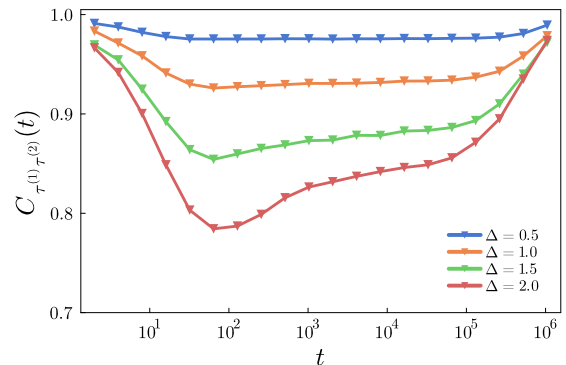


FIG. SM23: The correlation of the τ_i variables according to Eq. (SM30). $L = 16$ system annealed to zero temperature.

B.6 The two-time correlation

Finally, we have calculated the two-time correlation function, defined as

$$C(t, t_w) = \frac{1}{N} \sum_{i=1}^N [(s_i(t) s_i(t + t_w))] \quad (\text{SM31})$$

where $s_i(t) = \sigma_i(t) \tau_i(t)$ for the Δ -model and $s_i(t) = \sigma_i(t)$ for the EA one. As can be seen in Fig. SM24 the SWAP method induces a faster decay, compared to the single spin flip dynamics, in which the curves saturate rather quickly, consistent with plateau the R_p found in Fig. SM20.

B.8 Measures of frustration

In Fig. SM29 we follow the time evolution of the instantaneous configuration of the system, parametrized as its projection on the ground state of the final couplings $\mathcal{J}_{ij}^* = \mathcal{J}_{ij}(t_{\text{max}})$. More precisely, each square in the images represents

$$s_i(t) \sigma_i^{\text{gs}} = \tau_i(t) \sigma_i(t) \sigma_i^{\text{gs}}. \quad (\text{SM32})$$

The color code goes from -2 (light blue) to $+2$ (light red), A very negative value represents a long spin which

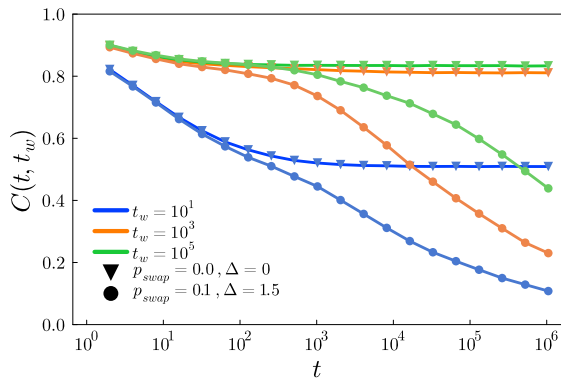


FIG. SM24: The two-time correlation of the s_i variables, confronting the SWAP method ($p_{\text{swap}} = 0.1$) with the $\Delta = 1.5$ -model with the single-spin-flip kinetics of the 2DEA model, both with sizes $L = 512$ and the waiting time values displayed in the key.

is anti-aligned with the ground state, while a very positive value represents a long spin which is aligned with the ground state. Dark squares represent short spins. On each vertex of the (dual) lattice we place a symbol when the corresponding plaquette of the original lattice is frustrated. The strength of the local frustration is quantified by

$$f_P(t) = \prod_{\langle ij \rangle \in P} \mathcal{J}_{ij}(t) = \prod_{\langle ij \rangle \in P} J_{ij} \tau_i(t) \tau_j(t). \quad (\text{SM33})$$

Concretely, on a square plaquette with site labels 1, 2, 3, 4,

$$f_P(t) = J_{12} J_{23} J_{34} J_{41} \tau_1^2(t) \tau_2^2(t) \tau_3^2(t) \tau_4^2(t). \quad (\text{SM34})$$

The sign, and whether the plaquette is frustrated or

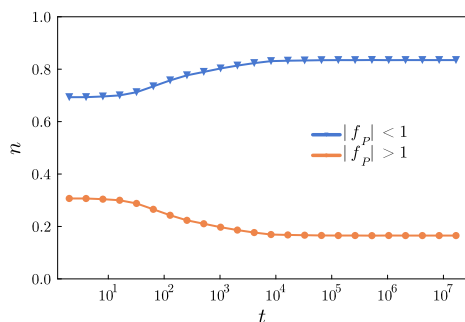


FIG. SM25: The number density of plaquettes with frustration $f_P < 0$, distinguished by the modulus being larger or smaller than 1.

not, is decided by the factor $J_{12} J_{23} J_{34} J_{41}$ while the magnitude of the potential frustration is determined by $\tau_1^2(t) \tau_2^2(t) \tau_3^2(t) \tau_4^2(t)$ which depends on time. Initially one can imagine that the last four factors are independent and $\tau_1^2 \tau_2^2 \tau_3^2 \tau_4^2 \sim (1 + \Delta^2/12)^4$. Going back to the snapshots, we used two kinds of symbols: a bullet for $|f_P(t)|$

greater than one, a triangle for $|f_P(t)|$ smaller than 0.1, respectively. We called n the density of each of these frustrated plaquettes, that is the number of the frustrated plaquettes of each kind divided by the total number of frustrated plaquettes N_F which is constant and approximately equal to half the total number of plaquettes.

A total frustration density, defined as the normalized sum of the local ones, reads

$$f(t) = \frac{1}{N_F} \sum_P f_P(t) \quad (\text{SM35})$$

with the sum running over frustrated plaquettes.

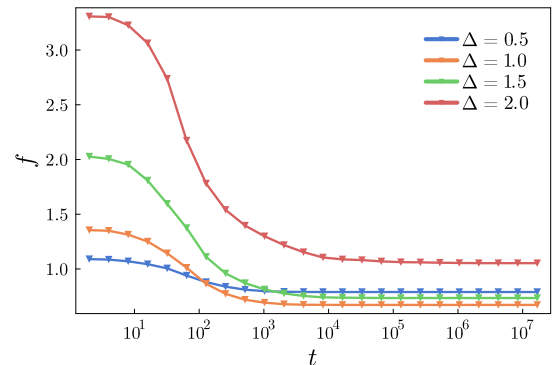


FIG. SM26: The magnitude of the total frustration f , defined in Eq. (SM35) in Δ -models with different values of Δ specified in the key and $L = 32$ quenched to zero temperature and evolved with SWAP. The initial value is $(1 + \Delta^2/12)^4$.

In the course of time we see the following.

- The frustrated or unfrustrated nature of the plaquettes does not change in time. When there is a symbol (bullet or triangle) attached to them, they do not disappear. They are not created elsewhere either.
- The strength of the local frustration does vary in time, so the symbols can change, for example, from bullet to triangle, or *vice versa*. The time dependence of the densities of frustrated plaquettes of each kind are shown in Fig. SM25. The number density of plaquettes with small frustration dominates over the ones with large frustration asymptotically.
- In the course of time the symbols rearrange spatially. Rather large regions with small frustration are visible in the late snapshots.
- The magnitude of the total frustration f tends to diminish in time.
- Initially, the color of the images is roughly randomly distributed over the full palette. In the course of time, blue cells tend to disappear and the

image becomes globally reddish. This means that the system orders in the direction of the selected ground state.

- In the last images the crosses (weak frustration) are located in regions where the spins have short length and the bullets (strong frustration) are placed in regions where the spins have long length.

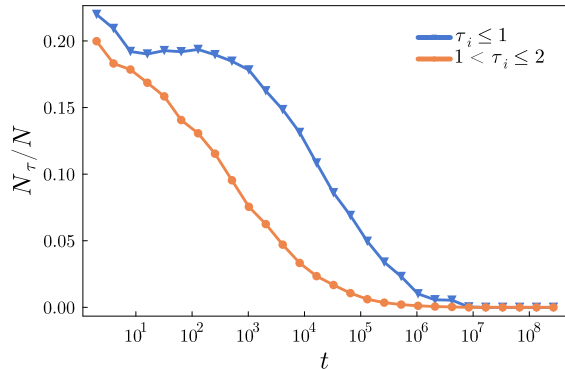


FIG. SM27: Time evolution for the ratio of small-length ($\tau_i \leq 1$) and large-length ($1 < \tau_i \leq 2$) spins with σ_i not aligned with the ground state σ_i^{gs} , i.e. $\sigma_i(t)\sigma_i^{\text{gs}} < 0$.

B.7 Instantaneous configurations

The mechanism that renders the SWAP method efficient in the frustrated Δ -Model is clarified by inspecting

some snapshots, as we did for the ferromagnetic model. In Fig. SM28, we show the actual configuration (first row) and the overlap with the ground state of the system with the final \mathcal{J}_{ij} interactions (second row). (In the main text we explain how we obtain the σ_i^{gs} configuration.) We have performed a sub-critical quench at $T = 0$, for $L = 128$ using SWAP dynamics with $p_{\text{swap}} = 0.1$.

The first row displays the spin configurations at four times after the quench. The images do not show much structure apart from a slight tendency of long spins with the same orientation to group locally. Still, and as expected, no structure with long-range spin ordering develops.

One can recognize the formation of domains in the overlap of the configurations with the ground state. Indeed, the images shown in the second row are primarily red or yellow, that is, the system acquires a positive overlap with the ground state all over space. The SWAP algorithm produces domain walls consisting mostly of short length spins (green and yellow). This structure lowers the energy barriers locally, making the spin-flip more feasible in these regions. The ratio of $\{\tau_i\}$ variables for which the corresponding Ising spins do not match the ground state (i.e. $\sigma_i(t)\sigma_i^{\text{gs}} < 0$) goes to zero, see Fig. SM27, in the course of time. However, the decay rate depends strongly on the length of the spins. Larger spins ($1 < \tau_i \leq 2$) align faster on the ground state directions compared to smaller ones ($\tau_i \leq 1$), as can also be seen in Fig. SM27, supporting the previous explanation.

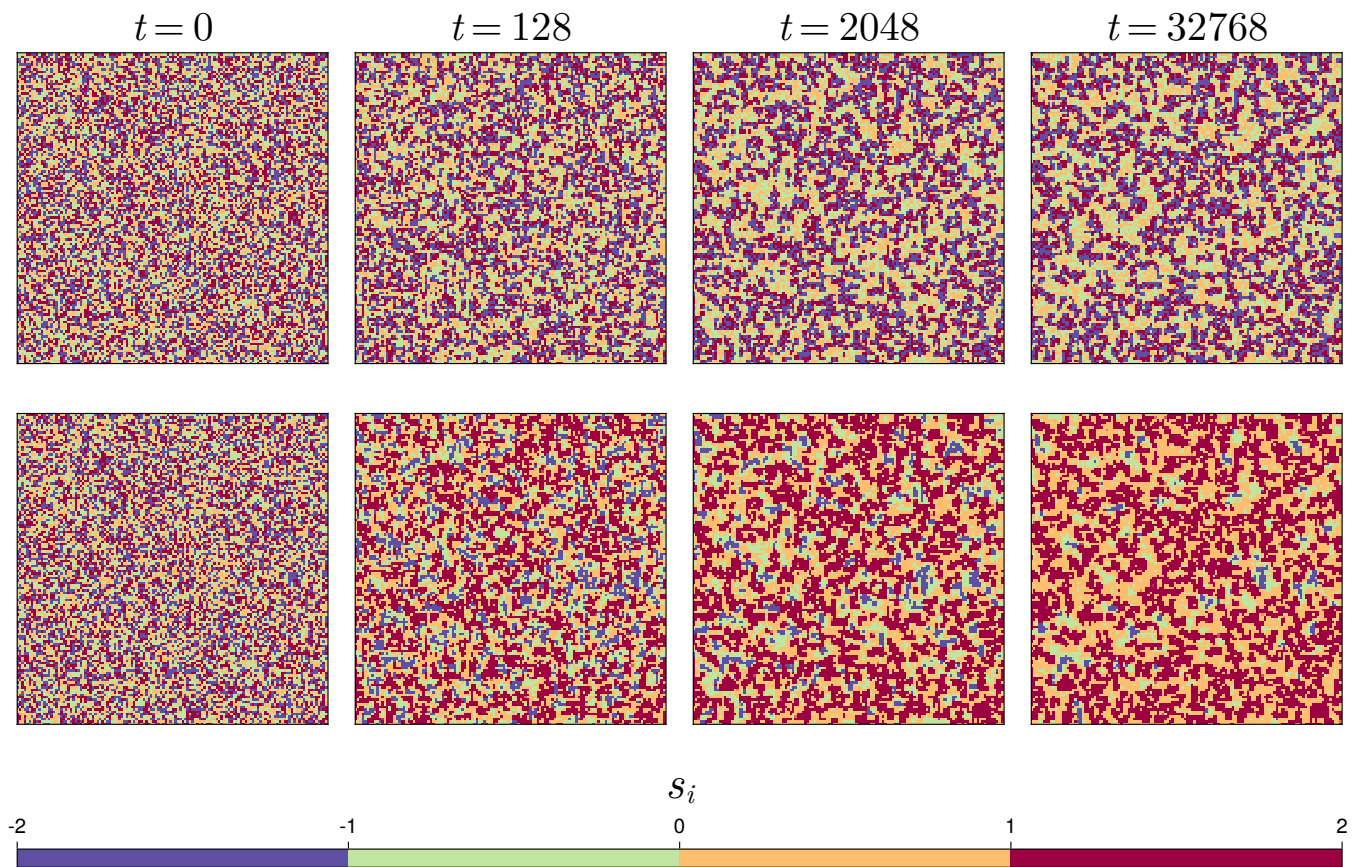


FIG. SM28: Instantaneous snapshots of the frustrated Δ -model with $\Delta = 2$, at four times indicated in the figure after a quench to $T = 0$. First row: The spin s_i configurations. Second row: Overlap with the σ -ground state $(s_i(t)\sigma_i^{\text{gs}})$. The color scale binned as indicated in the bar shows the lengths of the local spins.

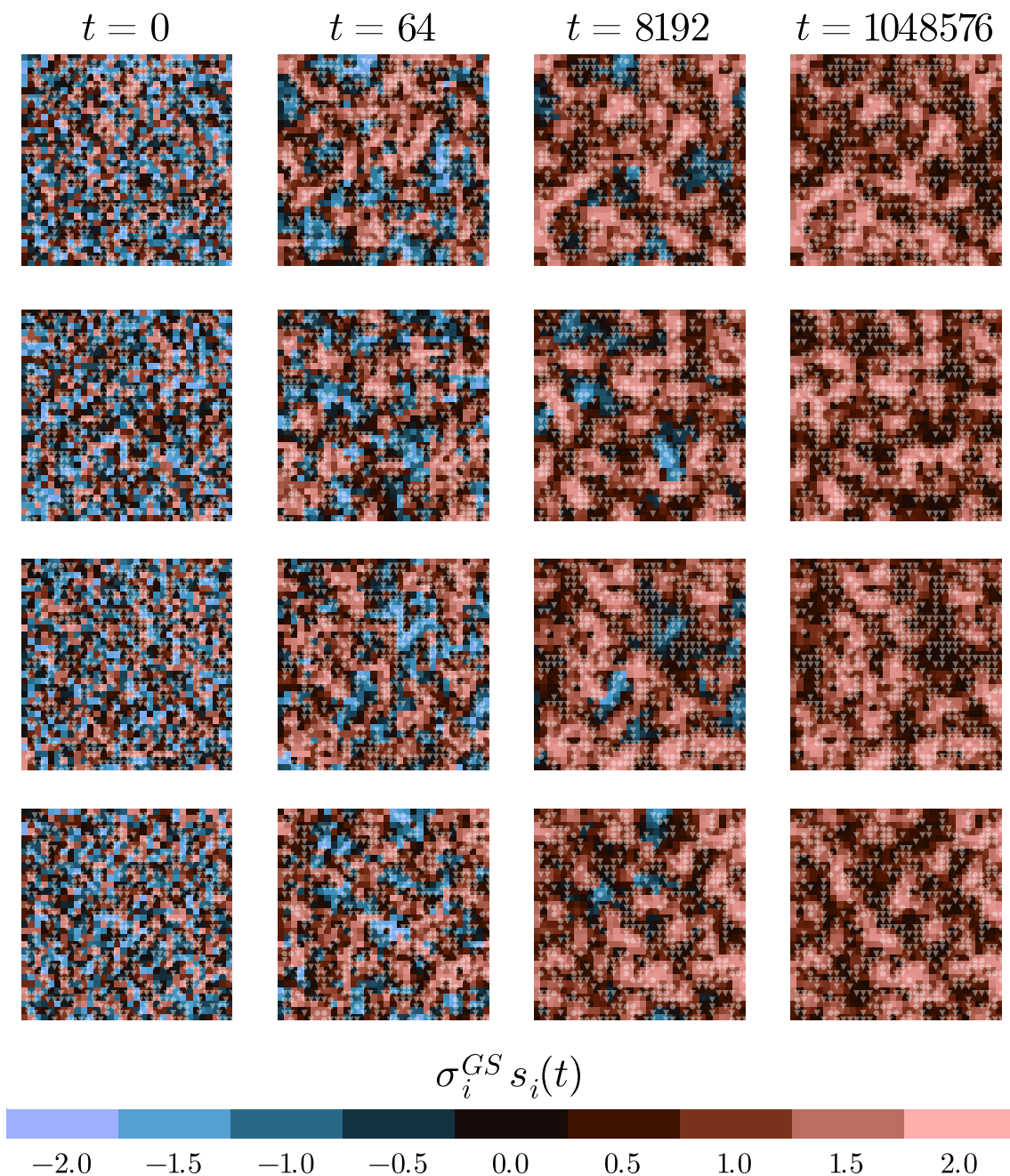


FIG. SM29: Instantaneous configurations of the Δ -model obtained at subsequent (though not equally spaced) times after a quench to $T = 0$ of four initial conditions (different rows) evolved with SWAP. Each square represents the instantaneous local overlap $\tau_i(t)\sigma_i(t)\sigma_i^{GS}$, see Eq. (SM32). The color code spans the interval $[-2$ (light blue), 2 (light red)]. The frustrated plaquettes are indicated with bullets and triangles according to the local frustration $f_P(t)$ being greater or smaller than one, respectively.